Journal Pre-proof

Fluorine-containing oxygen electrodes of the nickelate family for proton-conducting electrochemical cells

Artem P. Tarutin, Gennady K. Vdovin, Dmitry A. Medvedev, Aleksey A. Yaremchenko

PII: S0013-4686(20)30200-0

DOI: https://doi.org/10.1016/j.electacta.2020.135808

Reference: EA 135808

To appear in: *Electrochimica Acta*

Received Date: 5 September 2019

Revised Date: 28 January 2020

Accepted Date: 28 January 2020

Please cite this article as: A.P. Tarutin, G.K. Vdovin, D.A. Medvedev, A.A. Yaremchenko, Fluorine-containing oxygen electrodes of the nickelate family for proton-conducting electrochemical cells, *Electrochimica Acta* (2020), doi: https://doi.org/10.1016/j.electacta.2020.135808.

Fluorine-containing oxygen electrodes of the nickelate family for proton-conducting electrochemical cells

Artem P. Tarutin[a,b], Gennady K. Vdovin[a],

Dmitry A. Medvedev[a,b,*], Aleksey A. Yaremchenko[c,*]

[a] Laboratory of Electrochemical Devices Based on Solid Oxide Proton Electrolytes, Institute of High Temperature Electrochemistry, Yekaterinburg 620137, Russia
[b] Ural Federal University, Yekaterinburg 620002, Russia
[c] CICECO – Aveiro Institute of Materials, Department of Materials and Ceramic Engineering, University of Aveiro, 3810-193 Aveiro, Portugal
[*]Corresponding authors, e-mails: dmitrymedv@mail.ru (D.A. Medvedev) and ayaremchenko@ua.pt (A.A. Yaremchenko).

Abstract

In the present work, the anionic doping of a Ba-containing $Nd_2NiO_{4+\delta}$ mixed conductor is proposed as an efficient means of tuning its functional properties for application as an oxygen/steam electrode material in protonic ceramic electrolysis cells (PCECs). Single-phase $Nd_{1.9}Ba_{0.1}NiO_{4+\delta}F_\gamma$ (γ = 0, 0.03, 0.05, 0.07 and 0.1) nickelates having a K_2NiF_4-type structure were prepared and comprehensively characterised in the range from room temperature to 1000°C. A combination of complimentary techniques, including 4-probe DC electrical measurements, an electron-blocking method, electrochemical impedance spectroscopy and analysis of equivalent circuit schemes and distribution of relaxation times, was employed to reveal the fundamental correlations between electrical properties, oxygen-ionic transport and electrochemical performance of fluorinated nickelates. The highest ionic conductivity in combination with the lowest electrode polarisation resistance was found for the composition with γ = 0.05. The enhanced transport properties of this material were attributed to mixed anion lattice effect. Electrochemical tests of an electrolysis cell based on a proton-conducting $BaCe_{0.5}Zr_{0.3}Y_{0.1}Y_{0.1}O_{3-\delta}$ electrolyte with a $Nd_{1.9}Ba_{0.1}NiO_{4+\delta}F_{0.05}$ oxygen electrode demonstrated competitive performance compared to state-of-the-art PCECs, thus supporting the prospective viability of the proposed approach.

Keywords: F-doping; Nd_2NiO_4; proton-conducting electrolytes; PCECs & PCFCs; energy conversion; DRT analysis

Graphical abstract

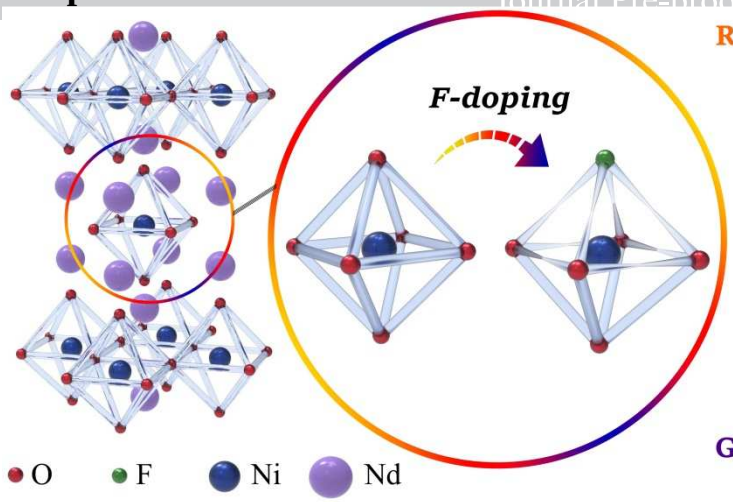

Repulsation between O^{2-} and F^{-} anions

Enhanced oxygen dynamic

Higher ionic conductivity

Lower overpotential values

Good oxygen(steam) electrode

1. Introduction

Proton-conducting electrochemical cells based on solid oxide materials are attractive energy conversion devices [1–4]. Such electrochemical systems meet a range of target criteria, including high efficiency, environmental friendliness and potential industrial application [5–8], which are crucial factors for the development of hydrogen and electrochemical energy technologies. Moreover, the working life of such cells can be extended compared with conventional solid oxide cells due to their low- and intermediate-temperature operation modes and consequently reduced rate of degradation processes [9–11]. However, in order to achieve commercially viable performance of protonic ceramic electrolysis cells (PCECs) and protonic ceramic fuel cells (PCFCs), their total resistances must be minimised by optimising the electrolyte and electrode components [12–15].

Complex oxides based on $Ln_2NiO_{4+\delta}$ (where Ln = La, Nd, Pr) have been intensively studied as possible oxygen / steam electrode materials for PCFCs/PCECs [16–20]. Of particular interest is their thermochemical compatibility with $Ba(Ce,Zr)O_3$-based proton-conducting electrolytes as well as good electrochemical activity towards electrochemical reactions involving water [16,21,22]. The utilisation of undoped $Ln_2NiO_{4+\delta}$ nickelates as electrodes is limited due to some drawbacks [23,24]; as a result, different doping strategies have been applied to optimise their functional properties. Among different strategies, the partial substitutions of Ln-ions by alkaline-earth elements M^{2+} (M = Ca, Sr, Ba [25–28]) or Ni-ions by copper, iron or niobium [29–32] can be highlighted as the most commonly adopted. At the same time, modification of the anionic sublattice is a relatively new and little explored approach to governing the target properties of complex oxides [33–35].

Regarding the functional materials that can be used in PCECs or PCFCs, the anionic modification of brownmillerite-type $Ba_2In_2O_5$-based protonic conductors using halogens has been intensively studied over the last decade by Animitsa et al. [36–40]. Later, F-, Cl- and Br-doping was used for classical $BaCeO_3$-based electrolytes having a perovskite structure [41–45]. However, studies of anionic modification of oxygen-conducting electrode materials for protonic ceramic

electrochemical cells are limited to only a few works [45,46] and need to be extended to gain a better understanding of the corresponding effects on electrode performance.

In the present work, we employed a solid-state approach to synthesise fluorinated $Nd_{1.9}Ba_{0.1}NiO_{4+\delta}F_{\gamma}$ nickelate electrode materials. Perovskite-type and perovskite-related oxyfluoride phases with high F contents are generally considered to be difficult to synthesise by means of high-temperature solid-state reaction due to the high stability of alkaline-earth fluorides AF_2 (A = Ca, Sr, Ba) and rare-earth oxyfluorides LnOF. Therefore, these materials are usually prepared by fluorination of oxide precursors at relatively low temperatures (≤ 400ºC) using a variety of fluorinating agents – F_2, XeF_2, NH_4F, MF_2 (M = Cu, Zn, Ni, Ag), or poly(vinylidenefluoride) [47,48]. Nevertheless, there are numerous reports claiming the successful preparation of fluorinated oxides by means of high-temperature solid-state reaction using alkaline-earth fluorides as precursors. The examples include synthesis of cobalt- and iron-based hexagonal perovskites $Ba_6Co_6O_{16-\delta}F_{1-x}$ [49], $Ba_5Co_5O_{13-\delta}F_{1-x}$ [50] and $BaFeO_{3-\delta}F_x$ ($0.15 \leq x \leq 0.35$) [51], perovskite-type $SrCo_{0.9}Nb_{0.1}O_{3-\delta}F_{0.1}$ [52] and $La_{1-x}Sr_xMnO_{3-2x+\delta}F_{2x}$ (x = 0–0.5) [53], K_2NiF_4-type Sr_2FeO_3F [54], indates and scandates of different structural types – perovskite $BaScO_2F$ [55], Ruddlesden-Popper Ba_2InO_3F [56], $Ba_3In_2O_5F_2$ [57] and Ba_2ScO_3F [58], as well as Sr_3MO_4F (M = Al, Ga) [59] and $Ca_2Al_3O_6F$ [60] oxyfluorides. Since PCEC/PCFC electrodes are expected to operate at elevated temperatures, solid-state synthesis was the logical choice in this work.

Thus, the aim of the present work was a comprehensive study of the functional properties of the prepared $Nd_{1.9}Ba_{0.1}NiO_{4+\delta}F_{\gamma}$ nickelates and the evaluation of possible effects of anionic modification on the oxygen-ionic transport in these oxides and their electrochemical activity as oxygen electrodes for proton-conducting electrochemical cells.

2. Experimental

2.1. Synthesis of materials

$Nd_{1.9}Ba_{0.1}NiO_{4+\delta}F_\gamma$ (NBNFγ, where γ = 0, 0.03, 0.05, 0.07 and 0.1) nickelates were synthesised via the solid-state synthesis method using high-purity (≥ 99.5%) Nd_2O_3, $BaCO_3$ and NiO. BaF_2 was used as a source of fluorine. The corresponding powders were measured in strictly calibrated amounts (calculated according to **equation (1)**) and then mixed using a PULVERISETTE 7 planetary micro mill.

$$0.95\,Nd_2O_3 + \left(0.1 - \frac{\gamma}{2}\right)BaCO_3 + \frac{\gamma}{2}BaF_2 + NiO + \frac{1}{2}(0.05 + \delta + 0.5\gamma)O_2 \rightarrow Nd_{1.9}Ba_{0.1}NiO_{4+\delta}F_\gamma + \left(0.1 - \frac{\gamma}{2}\right)CO_2 \quad \textbf{(1)}$$

The obtained precursor mixtures were stepwise fired at 1050 °C (5 h) and 1100 °C (5 h) with intermediate milling. Following subsequent phase analysis, the synthesised powders were divided into two groups. The first group was used for the preparation of electrodes of symmetrical and electrolysis cells, while the second was used to fabricate the ceramic samples for electrical and dilatometry measurements.

The electrode slurry was prepared by mixing the synthesised NBNFγ powders with α-terpineol, ethyl cellulose and dibutyl phthalate (in weight ratio of 90:8:2) dissolved in ethanol media. The ceramic samples were obtained by uniaxial pressing at 250 MPa followed by sintering at 1350 °C for 5 h.

2.2. Characterisation of materials

The phase composition of prepared materials was determined by X-ray diffraction (XRD) analysis using a Rigaku D/MAX-2200VL diffractometer. The XRD patterns were obtained using the CuK_α-radiation in the angle range of 20°–85° ($\Delta = 0.02°$, $\Delta/\tau = 1°\ min^{-1}$). The XRD data were refined using Rietveld analysis (Fullprof software [61]).

Images of the ceramics surface and the PCEC's cross-section were obtained using the scanning electron microscopy (SEM) analysis on a TESCAN MIRA 3 LMU microscope supplied with an Oxford Instruments X-MAX 80 energy dispersive spectrometer.

The oxygen overstoichiometry (δ) in NBNFγ was analysed using the thermogravimetric method (STA 449 F3 Jupiter, Netzsch). First, the weight change of powdered samples was monitored on heating/cooling in flowing ambient air to calculate a relative change in δ. Then, the same powders were subjected to complete reduction in 50 vol.%H_2 in Ar to obtain the absolute values of δ at the initial (room temperature) conditions. The measurements were performed in the temperature range of 30–1000 °C with the isothermal equilibration of the samples weight during 1 h in the case of air atmosphere.

The thermochemical behaviour of the ceramic materials was studied dilatometrically (Netzsch DIL 402 PC) in static air in cooling regime starting from 1000 °C and ending at 100 °C with a cooling rate of 3 °C min^{-1}. Thermal expansion coefficients (TECs) were calculated using the obtained dilatometric curves.

Electrical conductivity was measured by means of a standard 4-probe DC method using bar-shaped ceramic samples in a temperature range of 100–900 °C, with a specially developed Zirconia-318 source serving as temperature and oxygen partial pressure controller [62]. The oxygen-ionic conductivity was measured using a Wagner-Hebb technique detailed in **Section 3.3.3**.

2.3. Fabrication and characterisation of symmetrical cells

Electrode formation was carried out using a spraying method followed by sintering at 1100 °C for 1 h. Symmetrical cells were fabricated using dense proton-conducting $BaCe_{0.5}Zr_{0.3}Y_{0.1}Y_{0.1}O_{3-\delta}$ (BCZYYb) electrolyte discs with a thickness of 0.8 mm; the composition of the electrolyte was selected based on our recent work [63]. The electrode slurries were sprayed on opposite sides of the electrolyte discs, dried and sintered at 1100°C for 1 h.

The electrochemical behaviour of electrodes was evaluated using electrochemical impedance spectroscopy (EIS) analysis. This analysis was carried out using an Amel 2550 potentiostat/galvanostat and a MaterialsM 520 FRA-box. The impedance spectra were collected under the following conditions: T = 500–750 °C, wet air atmosphere (pH_2O = 0.03 atm), f = $1\cdot10^{-3}$–$1\cdot10^{6}$ Hz, U_{AC} = 30 mV.

The polarisation resistance (R_p) values were calculated as half (symmetrical configuration) of the difference between resistances corresponding to intersecting the real resistances axis with the measured impedance spectra.

2.4. Fabrication and characterisation of the protonic ceramic electrolysis cell

A Ni-cermet/electrolyte half-cell as a basis of the PCEC was prepared using the tape-calendering method as described in detail elsewhere [64]. The electrode slurry of optimal NBNFγ composition was applied onto the electrolyte surface of the half-cell (active area of 0.28 cm^2) and sintered at 1100 °C for 1 h to obtain a well-adhered anode layer. A current collector of $LaNi_{0.6}Fe_{0.4}O_{3-\delta}$ (LNF) composition was used to ensure a good current distribution over the NBNFγ steam electrode [65,66]. The single PCEC was tested utilising a home-made electrochemical system. The voltammetric and EIS measurements were performed using the same potentiostat / galvanostat and FRA unit. The impedance spectra were collected under wet (pH_2O = 0.50 atm) air / wet (pH_2O = 0.03 atm) H_2 gradient in the frequency range of $1 \cdot 10^{-2}$–$1 \cdot 10^{5}$ Hz with an AC perturbation of 30 mV and applied DC voltage of ~1.0, 1.2 and 1.4 V.

3. Results and discussion

3.1. Phase composition and crystal structure

The XRD analysis of sintered NBNFγ ceramic samples showed formation of single-phase materials with orthorhombic K_2NiF_4-type structure (**Figures 1**, **S1** and **S2**a). The anionic modification of $Nd_2NiO_{4+\delta}$ was found to have a minor effect on the structural parameters (**Table 1**). No visible shifts in the positions of the XRD reflections were observed (**Figure 1b**); the calculated unit cell volume varied within a narrow range of $1 \cdot 10^{-3}$ nm^3 with the composition. This can be explained as follows. Firstly, the fluorine doping level in the prepared compositions is narrow, while oxygen and fluorine ions have rather close ionic radii. In particular, in Shannon's system [67], the ionic radius of O^{2-} is equal to 0.138 nm (coordination number (CN)

equals to 4, O1-positions) or 0.140 nm (CN = 6, O2-positions), while the ionic radius of F^- reaches 0.131 or 0.133 nm, respectively. Secondly, minor changes in the anionic sublattice are likely to have a limited effect on the average oxidation state (and consequent average ionic radius) of the variable-valence nickel cations.

Table 1. Refined structural parameters of $Nd_{1.9}Ba_{0.1}NiO_{4+\delta}F_\gamma$ nickelates.

Concentration of F, γ		**0**	**0.03**	**0.05**	**0.07**	**0.1**
Space group		Fmmm				
a, nm		0.5377	0.5378	0.5379	0.5380	0.5381
b, nm		0.5431	0.5431	0.5430	0.5428	0.5425
c, nm		1.2402	1.2403	1.2403	1.2404	1.2406
V×10^3, nm		362.17	362.27	362.27	362.23	362.16
Nd	x	0	0	0	0	0
	y	0	0	0	0	0
	z	0.360	0.360	0.360	0.360	0.3600
8i	Occ.	2.040	2.012	2.029	2.006	1.985
Ni	x	0	0	0	0	0
	y	0	0	0	0	0
	z	0	0	0	0	0
4a	Occ.	0.976	0.995	0.999	0.965	0.978
O1	x	0.25	0.25	0.25	0.25	0.25
	y	0.25	0.25	0.25	0.25	0.25
	z	0	0	0	0	0
8e	Occ.	2.080	2.111	2.120	2.077	1.923
O2	x	0	0	0	0	0
	y	0	0	0	0	0
	z	0.173	0.172	0.171	0.171	0.170
8i	Occ.	2.021	2.064	2.068	2.033	2.058
R_p, %		7.7	9.2	9.3	9.9	9.3
R_{wp}, %		13.3	14.3	13.3	14.7	16.9
R_{exp}, %		9.7	9.3	9.7	11.3	10.2
χ^2		1.9	2.4	1.7	1.7	2.7
R-Bragg, %		2.7	2.0	3.6	2.6	4.7

It should be noted that the presence of phase impurities (such as BaF_2) was detected neither in the XRD patterns nor by the microstructural (SEM/EDS) inspection of the ceramic samples. It may be expected therefore that solid-state synthesis promotes the formation of fluorinated oxide materials without a noticeable

deviation from the nominal fluorine content. The utilisation of other preparation techniques such as combustion synthesis methods [44–46,68] may result in the formation of fluorine-depleted compositions due to possible HF volatility at high temperatures.

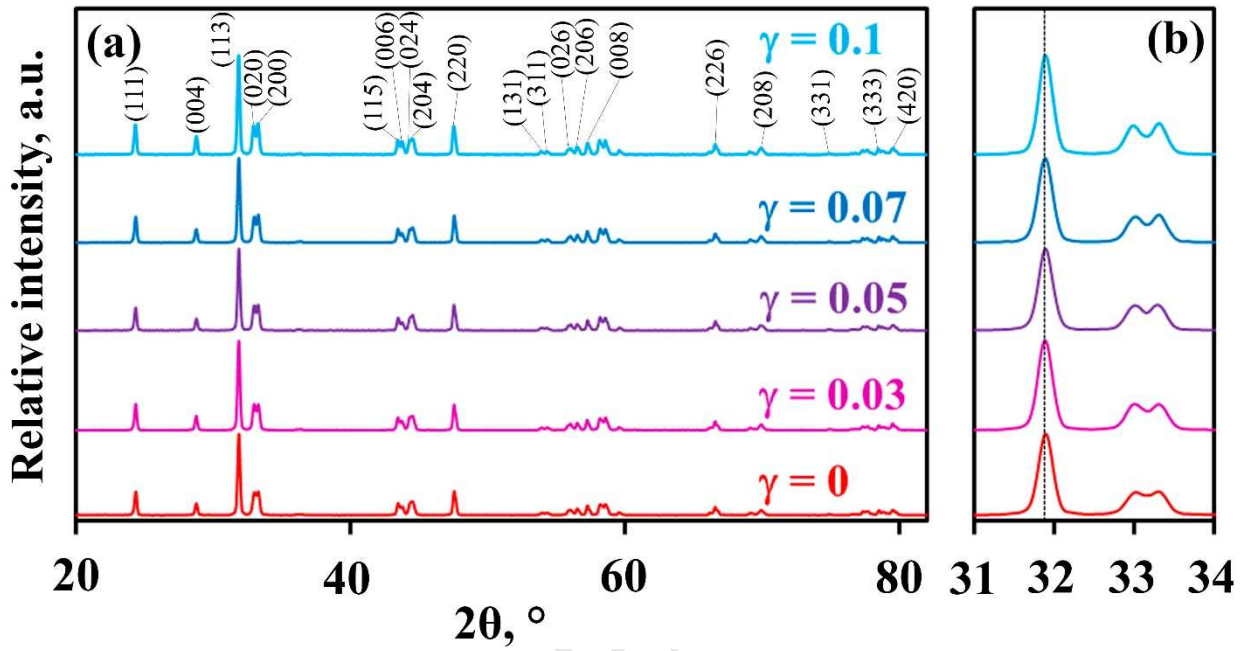

Figure 1. XRD patterns of the sintered $Nd_{1.9}Ba_{0.1}NiO_{4+\delta}F_{\gamma}$ ceramic samples: (a) in a wide 2θ range; (b) expanded view at 2θ = 31°–34°

3.2. Oxygen overstoichiometry

Oxygen-ionic transport in oxide materials, which is one of the key factors defining their electrical / electrochemical properties, depends both on the mobility of oxygen ions and their concentration. The latter can be determined by means of the TG technique.

The absolute level of the oxygen overstoichiometry (δ) in the reference state (room temperature) was calculated from the data regarding the weight loss of the NBNFγ powders upon their complete reduction on heating in H_2-containing atmosphere (**Figure 2a**). As it can be seen, the TG curves consist of five clearly distinguished regions:

1) The first region extends to 300–350 °C. This corresponds to a marginal weight loss, when the materials cannot be considerably reduced due to slow

reaction kinetics. Correspondingly, the oxygen concentration also changes insignificantly.

2) The second region, observed between 350 and 470 °C, corresponds to the reduction of Ni^{3+}-cations to the Ni^{2+} state. This process can be expressed (in conventional and quasi-chemical forms) by:

$$Nd_{1.9}Ba_{0.1}Ni^{2+}_{0.9-2\delta-\gamma}Ni^{3+}_{0.1+2\delta+\gamma}O_{4+\delta}F_{\gamma} \xrightarrow{[H]} Nd_{1.9}Ba_{0.1}Ni^{2+}O_{3.95-0.5\gamma}F_{\gamma} + \frac{(0.05+\delta+0.5\gamma)}{2}O_2 \qquad \textbf{(2)}$$

$$O_i^{//} + 2\,Ni_{Ni}^{\bullet} \xrightarrow{[H]} V_i^{x} + 2\,Ni_{Ni}^{x} + 1/2\,O_2 \qquad \textbf{(3)}$$

Here, $O_i^{//}$ is the interstitial oxygen ion and V_i^{x} is the interstitial vacancy, $Ni_{Ni}^{x} \equiv Ni^{2+}$, and $Ni_{Ni}^{\bullet} \equiv Ni^{3+}$ (i.e. the concentration of Ni^{3+} is equivalent to the concentration of electron-holes charge-compensating interstitial oxygen ions).

3) Ni^{2+}-ions possess tolerance towards the further reduction in the third region, within the temperature range of 470–550°C.

4) The fourth region in the TG curves (between 550 and 650 °C) corresponds to the complete reduction of Ni^{2+} ions to a metallic nickel and decomposition of NBNFγ:

$$Nd_{1.9}Ba_{0.1}Ni^{2+}O_{3.95-0.5\gamma}F_{\gamma} \xrightarrow{[H]} "Nd_{1.9}Ba_{0.1}O_{2.95-0.5\gamma}F_{\gamma}" + Ni^{0} + 0.5O_2 \qquad \textbf{(4)}$$

This yields a mechanical mixture of neodymium and barium oxides, fluorides and / or oxyfluorides (designated as "$Nd_{1.9}Ba_{0.1}O_{2.95-0.5\gamma}F_{\gamma}$").

5) No further weight changes occur in the last region, thus confirming the complete Ni^{2+}-to-Ni^{o} reduction at the previous stage.

Considering **equations (2)** and **(4)**, the δ value at room temperature as well as its change at other temperatures can be calculated, as shown in **Figure 2b**. In the case of NBNF0, the oxygen content at room temperature was calculated equal to ~4.24 oxygen atoms per formula unit (δ = 0.24), which is close to that for parent $Nd_2NiO_{4+\delta}$ [69–71].

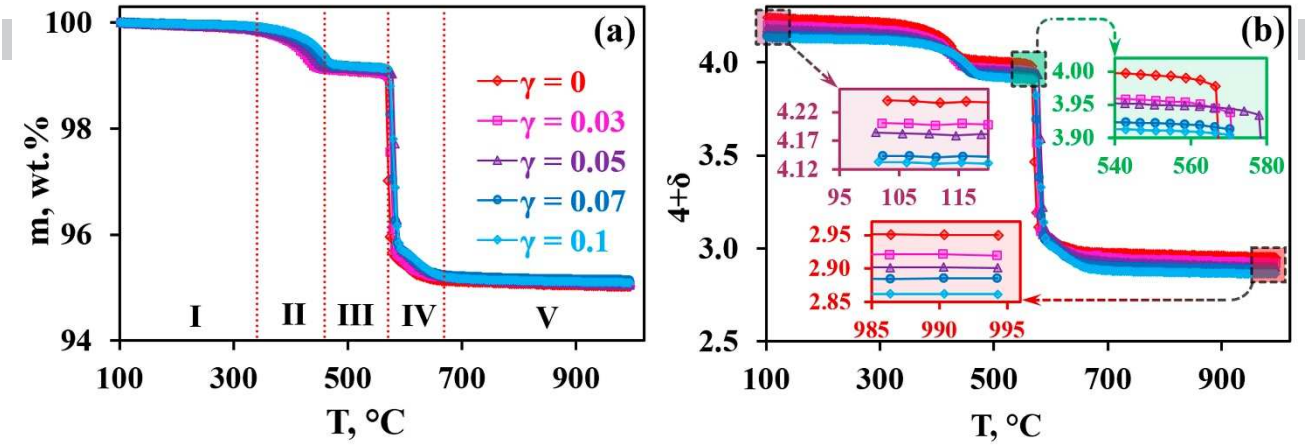

Figure 2. Thermogravimetric curves of $Nd_{1.9}Ba_{0.1}NiO_{4+\delta}F_{\gamma}$ powdered samples on heating in 50%H_2/Ar: (a) relative weight loss, and (b) corresponding changes in oxygen content (4+δ)

Variations of oxygen content on thermal cycling in air can be estimated on the basis of the known absolute value of δ at room temperature (assuming a fixed nominal fluorine content). As illustrated by **Figure 3a**, there are two common tendencies. Firstly, the nickelate lattice starts to lose oxygen (**equation (3)**) on heating above 300-400°C. This happens when the oxygen activity equilibrium between the sample and gas media is reached. The second tendency relates to a decrease in the overall oxygen content (4+δ) when the fluorine concentration increases in NBNFγ. Considering the intentional partial substitution of oxygen by fluorine (or BaO by BaF_2, **equation (1)**), this result is expectable.

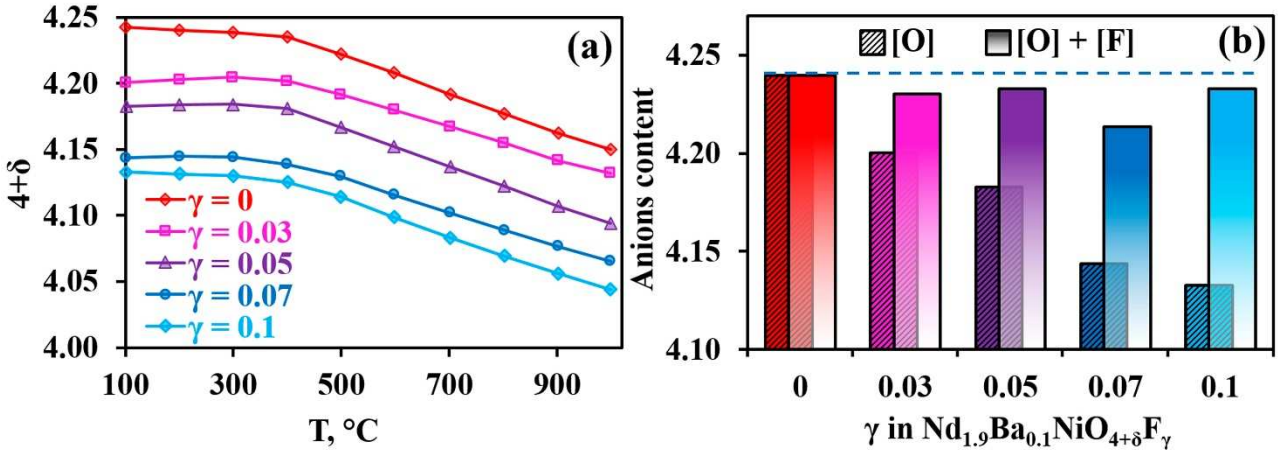

Figure 3. (a) Temperature dependency of oxygen content in $Nd_{1.9}Ba_{0.1}NiO_{4+\delta}F_{\gamma}$ nickelates in air, and (b) compositional dependency of oxygen and overall anion content in these phases at room temperature

In all cases, the calculated oxygen content exceeds 4 atoms per formula unit implying that the NBNFγ materials are oxygen over-stoichiometric phases in the entire studied range of temperature and fluorine concentration. It is interesting to note that the overall concentration of anions (**Figure 3b**) is virtually the same ($4+\delta+\gamma \approx 4.235 \pm 0.005$ at room temperature), except in the case of $\gamma = 0.07$, when a certain deviation ($4+\delta+\gamma \approx 4.21$) is observed.

3.3. Functionality of the $Nd_{1.9}Ba_{0.1}NiO_{4+\delta}F_{\gamma}$ materials

3.3.1. Thermomechanical properties

Thermomechanical behaviour is considered as one of the most important properties required for joint application of different materials in multi-layered structures, especially at elevated temperatures. Dilatometry may be effectively used to reveal possible phase transitions and determine thermal expansion coefficients (TECs) under dynamically changing conditions (temperature).

From the viewpoint of TECs, Ni-based oxides with layered structures are promising candidate components for PCFC/PCEC due to having much lower TEC values as compared with Fe- and Co-based oxides with perovskite-type structures [72]. According to **Figure 4a**, the dilatometric curves of all the NBNFγ materials demonstrate a smooth behaviour, although a phase transition from orthorhombic (sp. gr. Fmmm) to tetragonal (sp. gr. I4/mmm) structure can be expected to occur on heating. In the case of undoped $Nd_2NiO_{4+\delta}$, this phase transition is detected between 560 and 640 °C depending on the δ level [71,73,74].

The average and differential TECs of NBNFγ ceramics were calculated according to the following expressions:

$$\alpha_{av} = \frac{1}{L_o}\frac{\Delta L}{\Delta T}, \quad \alpha_{diff} = \frac{1}{L_o}\frac{\partial(\Delta L)}{\partial T} \qquad \textbf{(5)}$$

where L_o is the initial length of a sample; ΔL is its linear change under temperature variation. The average (or integral) TEC values amount to around 13.6 ± 0.4 ppm K^{-1} for all the studied materials, when a wide temperature range of 100–1000 °C is considered. Since no changes in the cationic sublattice occurred with the F-doping,

such insignificant deviations might be explained by the mentioned rigidity of the cationic framework of NBNFγ.

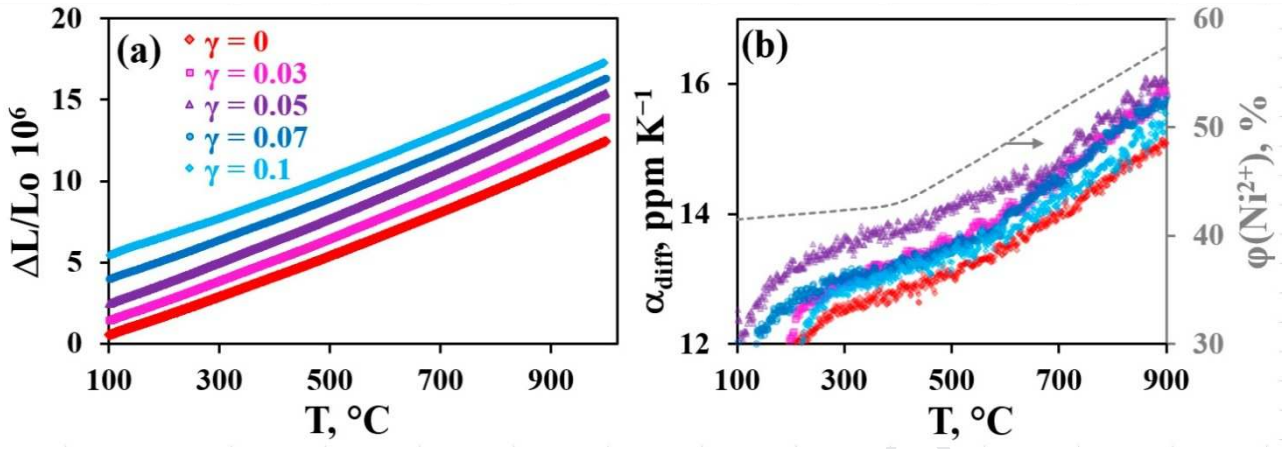

Figure 4. (a) Dilatometric curves of $Nd_{1.9}Ba_{0.1}NiO_{4+\delta}F_{\gamma}$ ceramics in air (shifted along Y axis for clarity), and (b) temperature dependency of differential TECs calculated from the dilatometric data. Dotted line in (b) shows the temperature dependency of Ni^{2+} fraction in the nickel sublattice of NBNF0

As it can be seen in **Figure 4b**, the differential TECs are also close at any selected temperature. Moreover, although disagreeing with some literature results on the related materials, in which TECs are found to be constant at the temperature variation [75], they are observed to decline as the temperature decreases. This anomaly can be attributed to insignificant changes in the oxygen overstoichiometry. In the present case, the 4 + δ level decreases with heating (**Figure 3a**), which causes a reverse increase in the Ni^{2+}-ions concentration (**equation (2)**, **Figure 4b**). Within the same coordination state, the reduced cations have higher ionic radii than their oxidised counterparts [67]. This initiates a chemical expansion effect, which results in an increase in differential TECs at higher temperatures [76].

Nevertheless, even under extreme conditions corresponding to the highest differential TECs (~16 ppm K^{-1} at 900 °C), the NBNFγ materials have a distinct advantage over the Fe- and Co-based complex oxides. As a rule, the integral TECs for the latter oxides exceed 20 ppm K^{-1}, while the chemical strain may increase the

differential TECs up to the particularly undesirable levels of 30–40 ppm K^{-1} [65,77,78].

3.3.2. Electronic conductivity

In order to be used as electrodes of solid oxide electrochemical cells, the NBNFγ materials should provide a good combination of high electronic and high ionic conduction, since they both promote fast electrochemical reactions.

The contribution of oxygen-ionic transport to the total electrical conductivity of $Ln_2NiO_{4+\delta}$ nickelates is known to be comparatively low. For instance, estimations of ionic transference numbers from the oxygen permeation data demonstrated that ionic conductivity in La_2NiO_4-based phases is 10^2 –10^4 times lower compared to electronic conductivity at 700–1000°C [79,80]. Therefore, one may reasonably assume that the total electrical conductivity of NBNFγ ceramics measured using a standard 4-probe DC method (**Figure 5**) is a predominantly electronic conductivity. The conductivity of NBNFγ as a function of temperature forms dome-type dependencies, when the conductivity grows and then drops with a gradual temperature rise (**Figure 5a**). The first part of these curves is associated with an increase in the electron hole mobility ($\mu_h, h = Ni_{Ni}^{\bullet}$), while the corresponding concentration ($p = [Ni_{Ni}^{\bullet}]$) changes insignificantly (see the grey dotted line in **Figure 5a**). This is due to the close relationship between the electron hole concentration and the oxygen overstoichiometry [25,32], which also has a weak dependency on the temperature (below 300 °C, **Figure 3a**). It should be noted that the conductivity exhibits a semi-conducting behaviour over the low-temperature range (**Figure S3a**), with quite low characteristic activation energy values (**Figure S3b**). The second part corresponds to the metallic-like behaviour of conductivity caused by the existence of two simultaneous processes: a decrease in both the electron hole mobility and concentration. However, the latter effect prevails over the former having a substantial effect on conductivity deterioration.

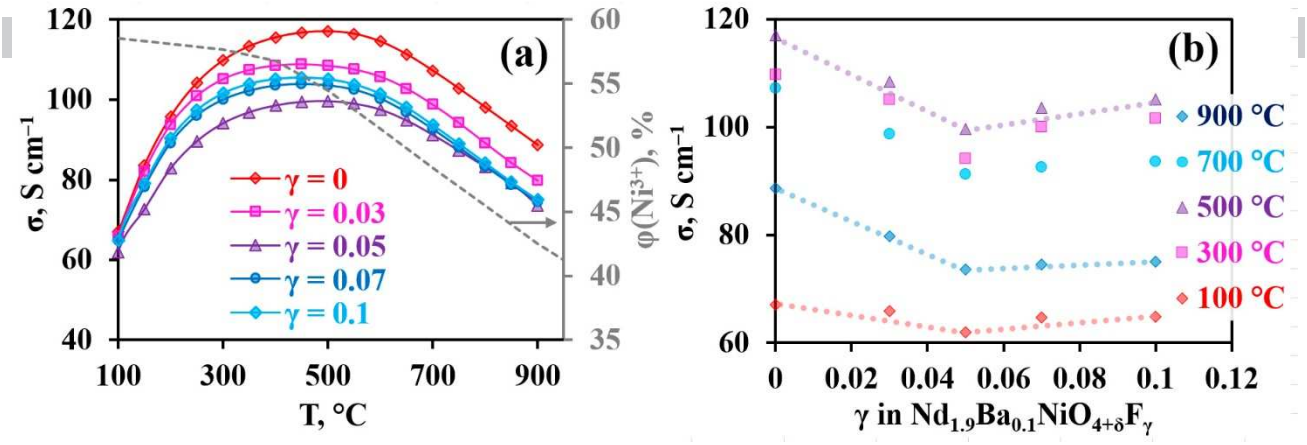

Figure 5. Electrical properties of $Nd_{1.9}Ba_{0.1}NiO_{4+\delta}F_{\gamma}$ ceramics in air: total electrical conductivity as a function of (a) temperature and (b) F-content. The dotted line in (a) shows the temperature dependency of Ni^{3+} fraction in the nickel sublattice of NBNF0.

By plotting the concentration-based curves of conductivity, the local minimum for $\gamma = 0.05$ can be revealed (**Figure 5b**). A possible reason for such a result will be proposed in the next section in terms of an analysis of the oxygen dynamics of the NBNFγ crystals.

3.3.3. Ionic conductivity

As mentioned above, the oxygen-ionic conductivity of the Ni-based Ruddlesden-Popper phases is typically several orders of magnitude lower than the electronic conductivity. As a result, the accurate determination of ionic conductivity in these materials requires the utilisation of more complex techniques (such as oxygen permeability and oxygen diffusivity measurements, blocking methods and others) [70,81,82]. In the present work, we took the electron-blocking approach, in which one component of the electrochemical system serves as an ionic filter with the result that electrons are not conducted (see **Figure S4**).

We used the following experimental sequence to determine the oxygen-ionic conductivity of NBNFγ. First, $Ce_{0.9}Gd_{0.1}O_{2-\delta}$ (gadolinia-doped ceria, GDC) ceramic materials were fabricated in the form of gas-tight discs with a thickness of ~2 mm. The GDC composition was selected due to its high and unipolar oxygen-ionic

conductivity under oxidising atmospheres at elevated temperatures [83,84]. The *p*-type electronic contribution to the total conductivity of doped ceria under these conditions is very limited (electron-hole transference number $t_p \approx 0.005$ at 900 °C and 0.0015 at 700 °C in the case of $Ce_{0.8}Gd_{0.2}O_{2-\delta}$) [85–87] and, therefore, was neglected in this work. Both sides of the GDC disc were thoroughly polished. The porous platinum (Pt) electrodes were symmetrically painted on the opposite sides of the disc, sintered at 1050 °C for 1 h and catalytically activated by an ethanol solution of $Pr(NO_3)_3$. Then the resistance of the GDC discs was calculated according to the Ohm equation:

$$R_{GDC} = \frac{U}{I} \cdot S \qquad \textbf{(6)}$$

Here, U is the voltage drop (U = 100, 200 and 300 mV), I is the passing current, and S is the electrode surface area.

In order to fabricate the two-layered system, the Pt electrode was carefully removed from one side of the GDC disc by polishing to form a nearly mirror-polished surface. This surface was then brought into close contact with the mirror-polished surface of a 1.5 mm-thick NBNFγ disc onto the other side of which a porous Pt electrode was applied. These two discs were subjected to a certain external pressure and heated to melt the high-temperature borosilicate glass (placed as shown in **Figure S4**) so as to avoid any contact between the ambient gas and the space between two contacting surfaces. The resistance of the two-layered glued systems was also determined according to the equation:

$$R_{total} = \frac{U'}{I} \cdot S \qquad \textbf{(7)}$$

On the basis of these two known resistances, as well as the thickness of the NBNFγ discs (H), the oxygen-ionic conductivity can be finally calculated:

$$\sigma_{ion} = \frac{H}{S} \cdot \frac{1}{R_{total} - R_{GDC}} \qquad \textbf{(8)}$$

Here, the U, U' and I levels were measured by the Keithley digital multimeters.

Figure 6 displays the obtained experimental data. The results show that the oxygen-ionic conductivity of the studied materials varies in the wide range from 2×10^{-4} to 9×10^{-2} S cm^{-1} depending on the temperature and fluorine content.

It is seen that the oxygen-ionic conductivity exhibits thermo-activated nature, with the characteristic activation energies of 1.06–1.25 eV (**Figure 6b**). The obtained values are consistent with the activation energies of oxygen diffusion of the $Ln_2NiO_{4+\delta}$-based oxides [88]. As a reminder, such a correlation should indeed be observed according to the Nernst-Einstein equation. Considering the absolute level of the oxygen-ionic conductivity, this correlates with data for other nickelates [70,89].

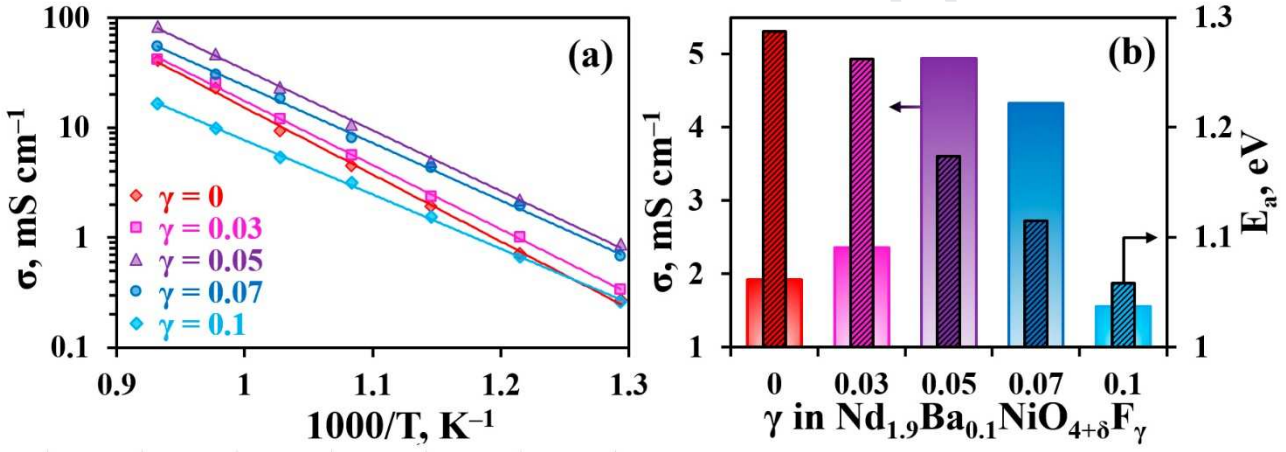

Figure 6. (a) Temperature dependency of partial oxygen-ionic conductivity of $Nd_{1.9}Ba_{0.1}NiO_{4+\delta}F_\gamma$ nickelates in air; (b) ionic conductivity (600 °C) and corresponding values activation energy (500–800 °C) vs fluorine content

In the isothermal regime, the oxygen-ionic conductivity of NBNFγ tends to increase from γ = 0 to γ = 0.05 and then to drop with a further increase in γ. This is correct for almost all the studied temperatures and may indicate the realisation of two competing effects.

At low γ levels, the enhancement of conductivity suggests a mixed anion effect, which is confirmed and described in detail by Animitsa's group for a wide range of F- and Cl-doped complex oxides [90–94]. There might be several reasons for appearance of this effect: changing the electron density of oxygen ions affected the binding energy and ionicity of M–O bonds, and electrostatic repulsion of different

anions located within one or neighbouring octahedrons, which seems to have a defining contribution. According to the mixed anionic effect concept, the ionic transport enhancement is observed at small concentrations of F- or Cl-ions, where the F^--contribution to the ion transport is negligible, but the repulsion energy becomes considerable.

At the higher γ levels, the concentration of mobile (interstitial) oxygen defects consequently decreases (**Figure 3**), which leads to a natural drop in ionic conductivity. Moreover, the mobility of oxygen-ions can be also diminished due to an overlapping of the migration paths between F^-- and O^{2-}-ions [93].

It should be mentioned that ionic conductivity can be measured via the blocking method if the ceramic materials exhibit a gas-tight structure. As can be seen from **Figure S5**, all sintered materials are highly dense (their relative density exceeds 95%) with no visible pores. Moreover, close relative densities allow the total conductivities to be considered as correct data, which do not require additional corrections taking the porosity of the samples into account [95].

In conclusion of this section it should be mentioned that the performed experiments do not exclude the possible electrode polarisation effects in the determination of ionic conductivity, although they were purposefully minimised. Despite of this approximation, the provided discussion is valid since only one parameter (the NBNFγ composition of the electrochemical cells) has been changed, and the obtained results imply that the highest ionic conductivity is reached for NBNF0.05.

3.4. Performance of the $Nd_{1.9}Ba_{0.1}NiO_{4+\delta}F_\gamma$ electrodes: symmetrically designed cells

3.4.1. Polarisation behaviours of the $Nd_{1.9}Ba_{0.1}NiO_{4+\delta}F_\gamma$ electrodes

The fabricated symmetrical cells of NBNFγ|BCZYYb|NBNFγ were electrochemically characterised in wet air atmosphere between 500 and 750 °C, see **Figure 7**. The obtained impedance spectra show different behaviour depending on temperature or composition (**Figure 7a,b**), so for the initial evaluation only the

overall polarisation resistances were calculated and compared. As shown in **Figure 7c,d**, the R_p values drop in a range of 0.45–270 $\Omega\,cm^2$; the minimally achievable values are observed for the NBNFγ electrodes with $\gamma = 0.05$ (0.45 $\Omega\,cm^2$ at 750 °C and ~69 $\Omega\,cm^2$ at 500 °C). From a macroscopic viewpoint, an electrode's performance is correlated with the ionic conductivity of the material used in its fabrication, which should be as high as possible in order to ensure not only an excellent distribution of ionic current along with the electronic one determined by the electronic conductivity. Although NBNF0.05 has the lowest electronic conductivity (**Figure 5a,b**), it exhibits the highest (apparent) oxygen-ionic conductivity, σ_{ion} (**Figure 6**).

Comparing the EIS results with the data of the previous sections, the strictly reverse relation in the NBNFγ system is observed between ionic conductivity and the overall polarisation resistance. Despite the detrimental effect of the ionic transport, the apparent activation energy of the overall polarisation resistance increases gradually with increased the fluorine concentration (inset in **Figure 7c**), whereas the inverse tendency occurs for the ionic conductivity (**Figure 6b**). This can be explained by the fact that the electrode processes are multi-stage, which involve a number of elementary steps affecting the overall polarisation resistance and corresponding activation energy.

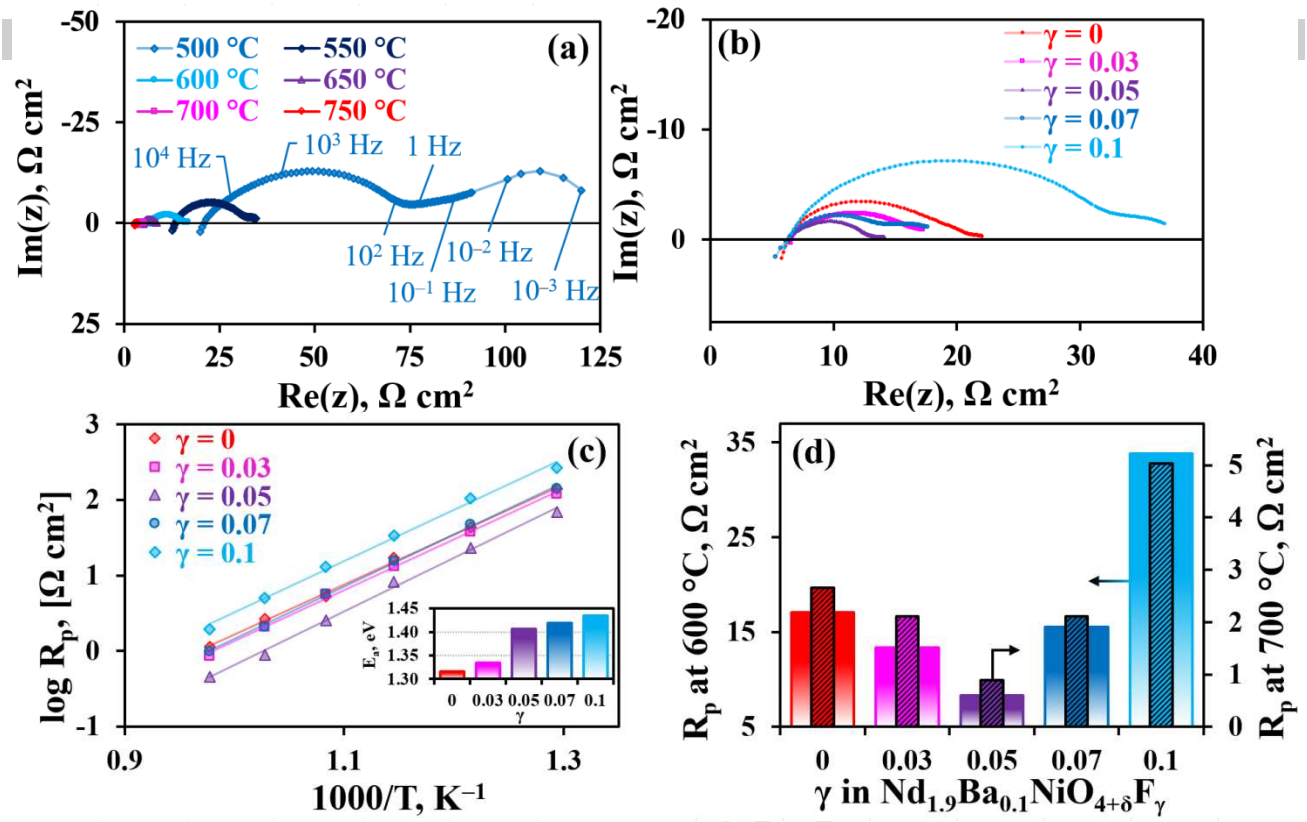

Figure 7. Electrochemical properties of $Nd_{1.9}Ba_{0.1}NiO_{4+\delta}F_{\gamma}$ electrodes: examples of impedance spectra of the symmetrical NBNFγ|BCZYYb|NBNFγ cells for (a) γ = 0.05 at various temperatures and (b) different NBNFγ electrodes at 600°C; (c) temperature-dependence of overall electrode polarization dependence; (d) overall polarisation resistance vs fluorine content at 700 and 600°C. Inset in (c) shows the values of activation energy of electrode process.

3.4.2. Detailed analysis of the $Nd_{1.9}Ba_{0.1}NiO_{4+\delta}F_{0.05}$ electrode performance

In order to reveal possible contributions to the electrodes response, we selected the most promising electrode, NBNF0.05, as well as providing the distribution of relaxation times (DRT) analysis. This analysis, which was carried out using a DRTtools software of Optimisation Toolbox MATLAB [96,97], is based on Tikhonov Regularisation method, enabling spectral deconvolution as well as a precise identification of separate processes corresponding to individual stages of the overall electrode process.

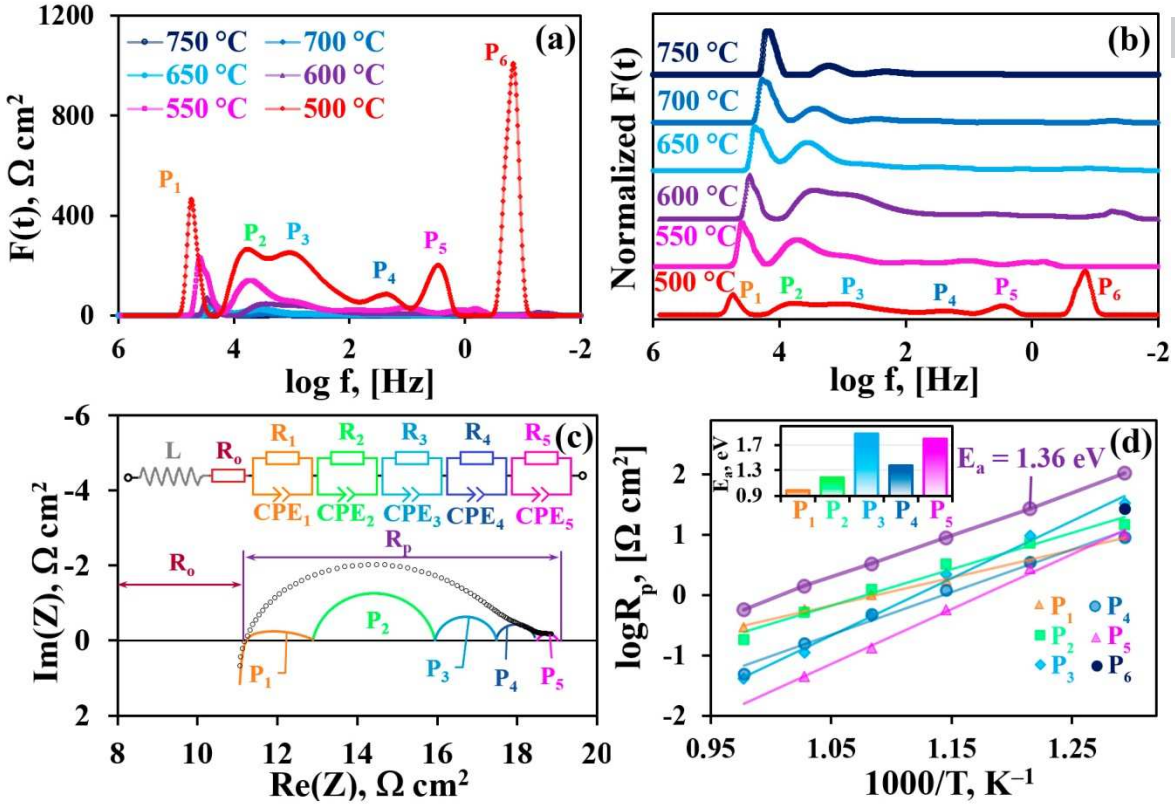

Figure 8. DRT analysis of the impedance spectra collected for the symmetrical cell with $Nd_{1.9}Ba_{0.1}NiO_{4+\delta}F_{0.05}$ electrodes: (a) a general view; (b) normalised DRT-functions; (c) an example of the spectra fitting using the determined values of R_1–R_5 at 600ºC; and (d) data on the partial polarisation resistances with corresponding values of activation energy.

The DRT-curves in general and normalised forms are presented in **Figure 8a,b**. These curves show a number of reflexes corresponding to the various stages of an electrode process. The following limiting processes can be distinguished: P_1 (with characteristic frequencies of 10–50 kHz), P_2 (4–11 kHz), P_3 (2–6 kHz), P_4 (2–150 Hz) and P_5 (60–400 mHz). Moreover, an additional stage P_6 appears at the lowest measured temperature, which is obviously not involved in the temperature evolution of the remaining reflexes.

The spectral deconvolution was performed on the basis of the area values under the DRT-peaks (**Figures S6 and 8c**) and the partial resistances were estimated (**Figure 8d**). According to the provided analysis, the electrode process is multi-stage and corresponds to the case when the overall polarisation resistance is determined by

three main elementary stages: P_1, P_2 and P_3 dominated at high, medium and low temperatures, respectively.

The P_1 stage, having a capacitance of 0.2–1 nF cm^{-2}, is assumed to be associated with oxygen-ionic [98,99] or protonic [100] transference through the electrolyte/electrode interface region. A resistance of this stage dominates at temperatures above 650 °C (**Figure S6**) having the lowest apparent activation energy values (**Figure 8d**).

The R_2 stage (1–10 nF cm^{-2}) might be attributed to the oxygen transport through the bulk of the NBNF0.05 electrode system [101,102]. The proximity of the apparent activation energies of this stage and ionic conductivity (1.17 eV, **Figure 6b**) confirms the proposed attribution. Although the achieved ionic conductivity is high, the > 20% contribution of P_2 resistance is also significant at all studied temperatures (**Figure S6**).

The P_3 process (7–60 nF cm^{-2}) prevails over other stages at 500 °C, but then rapidly decreases with heating. The oxygen reduction reaction may be responsible for this stage [66,103], which is catalytically improved as the temperature increases.

Other remaining processes (P_4 and P_5) may describe the surface association and desorption stages [102,104]. In particular, the very high apparent activation energy of oxygen desorption is close to that of the oxygen exchange constant of the nickelates (1.3–1.9 eV [105,106]).

The additional stage of P6 appears at temperatures below 550 °C (**Figure 8a**). This stage, involving a capacitance of about 0.2 F cm^{-2}, might describe the molecular diffusion of electrochemically active components in porous electrode media.

It should be mentioned that the DRT-reflexes shift towards low frequency values (**Figure 8b**), which is unusual for common systems [107,108]. However, this can be explained in terms of the changing nature of the electrode process, in which a hydrogen-involving mechanism is replaced by the oxygen-involving process accompanying a gradual increase in temperature. Indeed, it is widely known (see Table 4 in ref. [109]) that the $Ba(Ce,Zr)O_3$-based electrolytes behave as proton-conducting membranes at relatively low temperatures and tend to be co-ionic (at high temperatures) or predominately oxygen-ionic (at very high temperatures) conductors.

In this context, the highest electrochemical activity of the NBNF0.05 electrode might be associated with the highest oxygen-ionic conductivity, which accelerates the oxygen-involved electrochemical processes.

3.5. Characterisation of a protonic ceramic electrolysis cell based on the $Nd_{1.9}Ba_{0.1}NiO_{4+\delta}F_{0.05}$ electrode

3.5.1. Voltammetric characteristics and their analysis

The PCEC, LNF|NBFN0.05|BCZYYb|Ni–BCZYYb$_{funct.}$|Ni–BCZYYb$_{supp.}$, was electrochemically characterised starting with the volt-ampere analysis (**Figure 9**). In open circuit voltage (OCV) mode, this cell achieves voltages as high as 0.99 V at 600 °C and 0.90 V at 750 °C. However, these values are lower than those theoretically predicted (1.016 and 0.971 V, respectively), which were estimated for the 50% H_2O/air – 3% H_2O/H_2 conditions for an ideal hydrogen-concentration cell. An increase in differences between them at increasing temperatures indicates that the electronic transport in the BCZYYb electrolyte membrane is a key factor rather than any faultiness in the system's gas tightness (the cell maintains excellent integrity after electrochemical tests, see **Figure 12**).

The voltammetric dependencies of this cell suffer from the activation-like overpotential, especially pronounced at lower temperatures, causing their deviation from a linear behaviour (**Figure 9a**). Nevertheless, the current density of the PCEC in the thermo-neutral voltage mode (TNV, U ≈ 1.3 V) is quite high: 360, 750, 1370 and 1800 mA cm^{-2} at 600, 650, 700 and 750 °C, respectively. The reached values compete with those obtained for the state-of-the-art PCECs presented in **Table 2**, implying the appropriate fabricating technology and materials used.

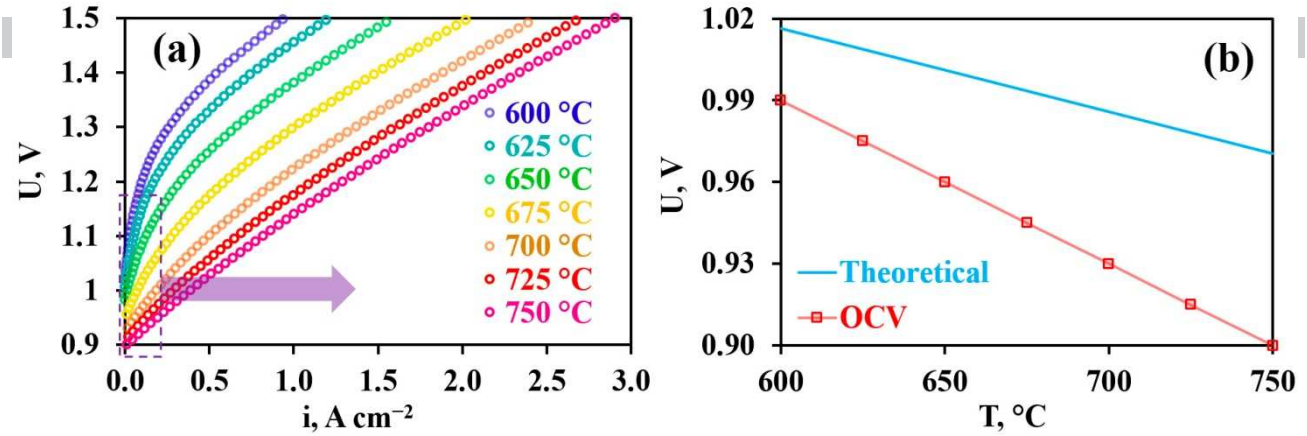

Figure 9. Electrochemical characteristics of the designed PCEC: (a) voltammetric curves at different temperatures, and (b) theoretical and measured open circuit voltage vs temperature

3.5.2. Electrode performance

To assess the electrochemical activity of the electrodes, the EIS analysis was employed at different temperatures and applied DC voltages (**Figure 10**).

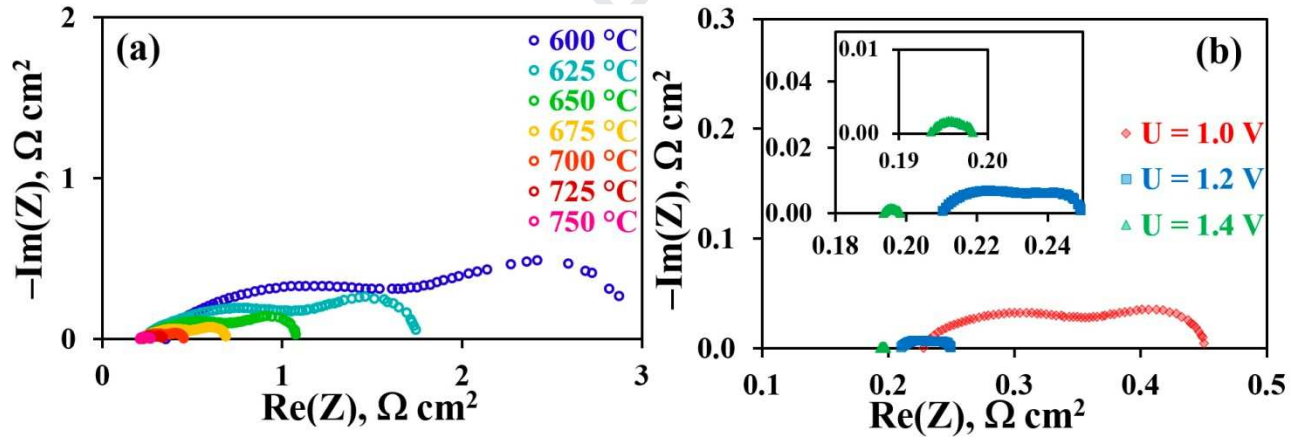

Figure 10. Electrochemical response of the PEFC: original impedance spectra obtained (a) under U = 1.0 V at different temperatures and (b) at 700 °C at different applied DC voltage. The detailed data on the evolution of the impedance spectra with temperature are detailed in **Figure S7**.

When the condition close to OCV operation mode was studied (**Figures 10a** and **S7**), these spectra demonstrated similar qualitative behaviour to those measured for the symmetrical cell (**Figure 8**). Although such a correlation indicates that the overall polarisation resistance of the PEFC is determined by the oxygen (steam) electrode,

i.e. NBNF0.05, a response from the hydrogen electrode can be distinguished. The comparison of the corresponding DRT spectra also reveals the same characteristic fragments (**Figure S8**), which agrees with the provided statement.

The absolute R_p levels of the PCEC under U = 1.0 V (close to OCV mode) are not rather high: only 2.59 Ω cm^2 at 600 °C and 0.23 Ω cm^2 at 700 °C. For example, among the PCECs under consideration (**Table 2**), the lowest R_p values of 0.50 Ω cm^2 at 600 °C and 0.13 Ω cm^2 at 700 °C are reached for the $Sr_{2.8}La_{0.2}Fe_2O_{7-\delta}$ [113] and LSN – Cu-doped BCZYYb [112] electrodes, respectively. It is evident that the mentioned activation-like polarisation effect is the main reason for the insufficient electrode performance under OCV mode of operation. However, when operation conditions of the PCEC were shifted from the OCV conditions, a considerable improvement was observed (**Figure 10b**). In detail, when the bias was increased from 1.0 to 1.4 V, the R_p values decreased down to 0.011 Ω cm^2 at 600 °C and 0.005 Ω cm^2 at 700 °C. Therefore, they may compete with the best data presented in **Table 2**.

In order to reveal possible reasons for the improvement of electrode performance under increasing bias, DRT analysis was also utilised. As shown in **Figure S9**, the absolute values of the partial polarisation resistances decrease noticeably as the bias increases. This is in line with the recently obtained data [110,116], which imply improved electrode kinetics in the PCECs towards water dissociation and hydrogen production. It is interesting to note that the low-frequency processes start to disappear with increasing bias; at the same time, the remaining reflexes shift to the low-frequency range. These two facts might indicate that the processes are accelerated with participation of hydrogen particles, while the oxygen-based electrochemical stages with a low relaxation time become dominant. In this regard, we would like to again highlight that the transport nature of the electrolytes in protonic ceramic electrochemical cells, as well as the electrochemical behaviour of the electrodes, is changeable with variation in temperature or bias [117,118].

Table 2. Design and performance of PCECs under open circuit voltage (OCV) and in thermo-neutral voltage mode (TNV, U ≈ 1.3 V): h is the electrolyte thickness, E_H is the theoretical voltage level of the ideal proton-conducting cells, E_{OCV} is the open circuit voltage value, i is the current density.

Electrolyte		**Oxygen electrode**	**Gases composition**	**T, °C**	**E_H, V**	**OCV mode**	**TNV mode**	**Ref.**
Composition	**h, μm**					**E_{OCV}, V**	**i, mA cm^{-2}**	
BCZYYb	26	$Nd_{1.9}Ba_{0.1}NiO_{4+\delta}F_{0.05}$	3%H_2O/H_2 – 50%H_2O/air	600	1.02	0.99	360	This work
				700	0.99	0.93	1370	
$BaCe_{0.7}Zr_{0.1}Y_{0.2}O_{3-\delta}$ (BCZY)	15	$SrEu_2Fe_{1.8}Co_{0.2}O_{7-\delta}$	3%H_2O/H_2 – 10%H_2O/air	600	1.09	0.99	400	[110]
				700	1.07	0.95	1050	
BCZY	15	$La_{1.2}Sr_{0.8}NiO_{4+\delta}$ (LSN)	3%H_2O/H_2 – 20%H_2O/air	600	1.06	1.01	420	[16]
				700	1.03	0.98	1370	
BCZY	16	LSN	3%H_2O/H_2 – 20%H_2O/air	600	1.06	1.02	420	[111]
				700	1.03	0.98	1410	
Cu-doped $BaCe_{0.7}Zr_{0.1}Y_{0.1}Yb_{0.1}O_{3-\delta}$ (BCZYYb10)	13	LSN – Cu-doped BCZYYb10	3%H_2O/H_2 – 20%H_2O/air	700	1.03	1.02	1960	[112]
$BaCe_{0.6}Zr_{0.2}Y_{0.2}O_{3-\delta}$ (BCZY20)	20	$Pr_2NiO_{4+\delta}$ – BCZY20	H_2 – 40%H_2O/air	600	1.03	0.98	220	[18]
				700	1.00	0.93	950	
$BaCe_{0.5}Zr_{0.3}Y_{0.2}O_{3-\delta}$	20	$Sr_{2.8}La_{0.2}Fe_2O_{7-\delta}$	3%H_2O/H_2 – 20%H_2O/air	600	1.06	0.96	460	[113]
				700	1.03	0.92	1080	
$BaCe_{0.4}Zr_{0.4}Y_{0.1}Yb_{0.1}O_{3-\delta}$	15	$PrBa_{0.5}Sr_{0.5}Co_{1.5}Fe_{0.5}O_{5+\delta}$	3%H_2O/H_2 – 3%H_2O/air	600	1.13	1.03	1920	[114]
BCZYYb10	15	$Pr_2NiO_{4+\delta}$	H_2 – 60%H_2O/air	600	1.00	0.99	630	[115]
				700	0.98	0.95	1670	

3.5.3. Microstructural analysis

The electrochemically tested PCFC was characterised by the SEM analysis. It was found that PCFC maintains its gas-tightness, as well as the adherence of joining materials. According to **Figure 11**, the fuel and steam electrodes are highly porous, while the electrolyte remains in a dense form, providing excellent separation of oxidising and reducing atmospheres. The thicknesses of the Ni–BCZYYb functional cathode, BCZYYb electrolyte, NBNF0.05 anode and LNF current collector layers are estimated to be equal to around 30, 26, 12 and 30 µm, respectively. The total thickness of the PCEC (including the supported cathode) is around 800 µm. The relatively homogeneous distribution of main cations corresponds to the desirable phases. Therefore, the integrity of the PCFC following its electrochemical characterisation provides evidence of the accuracy of the obtained data.

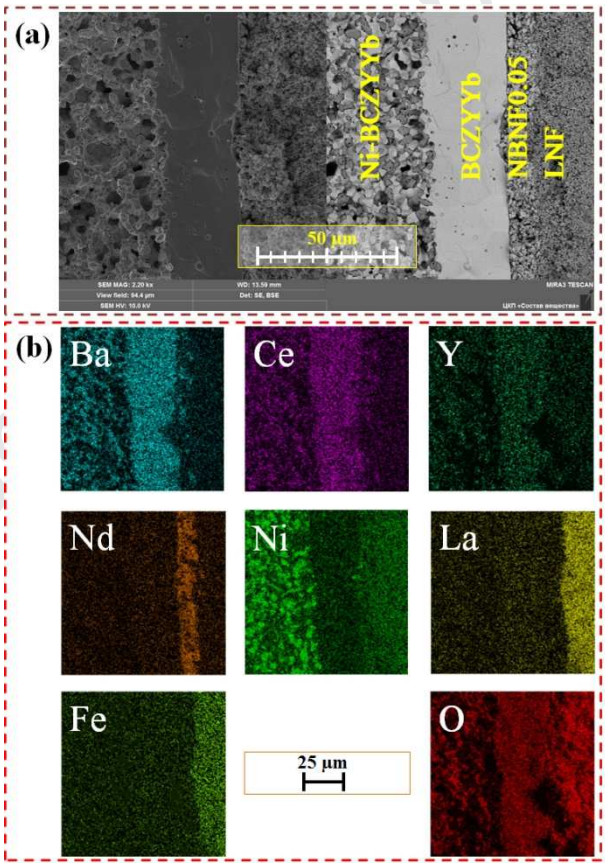

Figure 11. Microstructural analysis of the Ni–BCZYYb|BCZYYb|NBNF0.05|LNF protonic ceramic electrolysis cell after electrochemical testing: (a) cross-section in secondary (left) and back-scattered (right) electron imaging modes; (b) EDS maps of distribution of the main elements.

4. Conclusions

In the present work, new F-modified $Nd_2NiO_{4+\delta}$-based materials are proposed as promising oxygen (or steam) electrodes for application in protonic ceramic electrolysis cells (PCECs). To confirm the viability of $Nd_{1.9}Ba_{0.1}NiO_{4+\delta}F_\gamma$ (γ = 0, 0.03, 0.05, 0.07 and 0.1), a number of tasks have been resolved, including the production of single-phase materials, study of their composition (oxygen content, δ) features, functional properties (thermal expansion behaviour, electronic and ionic conductivities), as well as their electrochemical characteristics (polarisation behaviour of symmetrical and electrolysis cells). It was found that a slight F-doping of $Nd_{1.9}Ba_{0.1}NiO_{4+\delta}$ improves the ionic transport, presumably, due to the repulsion phenomenon occurring between oxygen and fluorine anions. The protonic ceramic electrolysis cell based on the most optimal composition, $Nd_{1.9}Ba_{0.1}NiO_{4+\delta}F_{0.05}$, exhibited a high hydrogen production rate of 5- and 11-ml min^{-1} cm^{-2} at 600 and 700 °C, respectively, at the applied voltage of 1.4 V; these levels compete with the best results reported for state-of-the-art PCECs.

In conclusion, the electrochemical properties of $Nd_{1.9}Ba_{0.1}NiO_{4+\delta}F_{0.05}$ open great prospects for the development of new electrode/electrolyte combinations allow a high performance of electrochemical devices to be achieved at reduced operation temperatures.

Acknowledgments

This work was supported by the Russian Foundation for Basic Research [grant no. 18-38-20063]. Dr. D. Medvedev is grateful to the Council of the President of the Russian Federation [scholarship no. СП-161.2018.1] for supporting the studies devoted to new MIEC materials, while Mr. A. Tarutin is grateful to the same foundation [scholarship no. СП-1413.2019.1] for supporting the studies aimed at new strategies of $Nd_2NiO_{4+\delta}$ modification. A.A. Yaremchenko would like to acknowledge financial support by the FCT, Portugal (project CICECO-Aveiro Institute of Materials, UIDB/50011/2020 & UIDP/50011/2020, financed by national funds

through the FCT/MEC and when appropriate co-financed by FEDER under the PT2020 Partnership Agreement).

The authors thank Dr. J. Lyagaeva and Mr. A. Farlenkov for their assistance in experiments performed.

The characterisation of powder and ceramic materials was carried out at the Shared Access Centre "Composition of Compounds" of the Institute of High Temperature Electrochemistry [119].

Declaration of interest

One of the authors (Dr. Dmitry Medvedev) acts as a Guest Editor of the special issue in which this article is to be published. All other authors declare no conflict of interest.

Author Contribution Statement

Conceptualization: D.M.; Methodology: A.T., G.V., D.M. and A.Y.; Validation: D.M.; Formal analysis: A.T., D.M. and A.Y.; Investigation: A.T., G.V. and D.M.; Resources: A.T. and G.K.; Writing – original draft preparation: A.T., D.M. and A.Y.; Writing – review & editing: D.M.; Visualization: A.T.; Supervision: D.M.; Project administration: D.M.; Funding acquisition: A.T., D.M. and A.Y.

References

[1] J. Kim, S. Sengodan, S. Kim, O. Kwon, Y. Bu, G. Kim, Proton conducting oxides: A review of materials and applications for renewable energy conversion and storage, Renew. Sustain Energy Rev. 109 (2019) 606. DOI: https://doi.org/10.1016/j.rser.2019.04.042.

[2] S. Hossain, A. M. Abdalla, Siti N. B. Jamain, J. H. Zaini, A. K. Azad, A review on proton conducting electrolytes for clean energy and intermediate temperature-solid oxide fuel cells, Renew. Sustain. Energy Rev. 79 (2017) 750. DOI: https://doi.org/10.1016/j.rser.2017.05.147.

[3] H. Dai, H. Kou, H. Wang, L. Bi, Electrochemical performance of protonic ceramic fuel cells with stable $BaZrO_3$-based electrolyte: A mini-review, Electrochemistry Communications 96 (2018) 11. DOI: https://doi.org/10.1016/j.elecom.2018.09.001.

[4] F.J.A. Loureiro, N. Nasani, G.S. Reddy, N.R. Munirathnam, D.P. Fagg, A review on sintering technology of proton conducting $BaCeO_3$-$BaZrO_3$ perovskite oxide materials for Protonic Ceramic Fuel Cells**,** J. Power Sources 438 (2019) 226991. DOI: https://doi.org/10.1016/j.jpowsour.2019.226991.

[5] S. A. Saadabadi, A. T. Thattai, L. Fan, R. E. F. Lindeboom, H. Spanjers, P. V Aravind, Solid oxide fuel cells fuelled with biogas: potential and constraints, Renew. Energy 134 (2019) 194. DOI: https://doi.org/10.1016/j.renene.2018.11.028.

[6] A. Buonomano, F. Calise, M. D. d'Accadia, A. Palombo, M. Vicidomini, Hybrid solid oxide fuel cells–gas turbine systems for combined heat and power: A review, Appl. Energy 156 (2015) 32. DOI: https://doi.org/10.1016/j.apenergy.2015.06.027.

[7] V. Venkataraman, M. Pérez-Fortes, L. Wang, Y. S. Hajimolana, C. Boigues-Muñoz, A. Agostini, S. J. McPhail, F. Maréchalc J. V. Herle, P.V. Aravind, Reversible solid oxide systems for energy and chemical applications – Review & perspectives, J. Energy Storage 24 (2019) 100782. DOI: https://doi.org/10.1016/j.est.2019.100782.

[8] J. Nowotny, J. Dodson, S. Fiechter, T. M. Gür, B. Kennedy, W. Macyk, T. Bak, W. Sigmund, M. Yamawaki, K. A. Rahman, Towards global sustainability: Education on environmentally clean energy technologies, Renew. Sustain. Energy Rev. 81 (2018) 2541. DOI: https://doi.org/10.1016/j.rser.2017.06.060.

[9] M. Ni, M. K. H. Leung, D. Y. C. Leung, Technological development of hydrogen production by solid oxide electrolyser cell (SOEC), Int. J. Hydrogen Energy 33 (2008) 2337. DOI: https://doi.org/10.1016/j.ijhydene.2008.02.048.

[10] I. Sreedhar, B. Agarwal, P. Goyal, S. A. Singh, Recent advances in material and performance aspects of solid oxide fuel cells, J. Electroanal. Chem. 848 (2019) 113315. DOI: https://doi.org/10.1016/j.jelechem.2019.113315.

[11] E. G. Kalinina, E. Yu. Pikalova, New trends in the development of the method of electrophoretic deposition in the SOFC technology: theoretical approaches, experimental solutions and development perspectives, Russ. Chem. Rev. 88 (2019) DOI: https://doi.org/10.1070/RCR4889.

[12] M. Abdalla, S. Hossain, A. T. Azad, P. M. I. Petra, F. Begum, S. G. Eriksson, A. K. Azad, Nanomaterials for solid oxide fuel cells: A review, Renew. Sustain. Energy Rev. 82 (2018) 353. DOI: https://doi.org/10.1016/j.rser.2017.09.046.

[13] Y. Wang, W. Li, L. Ma, W. Li, X. Liu, Degradation of solid oxide electrolysis cells: phenomena, mechanisms, and emerging mitigation strategies – a review, J. Mater. Sci. Technol. (2020) In press. DOI: https://doi.org/10.1016/j.jmst.2019.07.026.

[14] A. V. Kasyanova, L. R. Tarutina, A. O. Rudenko, Y. G. Lyagaeva, D. A. Medvedev, Ba(Ce,Zr)O_3-based electrodes for protonic ceramic electrochemical cells: towards highly compatible functionality and triple-conducting behaviour, Russ. Chem. Rev. 89 (2020). In press. DOI: https://doi.org/10.1070/RCR4928.

[15] W. Shi, J. Zhu, M. Han, Z. Sun, Y. Guo, Operating limitation and degradation modeling of micro solid oxide fuel cell-combined heat and power system, Appl. Energy 252 (2019) 113444. DOI: https://doi.org/10.1016/j.apenergy.2019.113444.

[16] S. Yang, Y. Wen, J. Zhang, Y. Lu, X. Ye, Z. Wen, Electrochemical performance and stability of cobalt-free $Ln_{1.2}Sr_{0.8}NiO_4$ (Ln=La and Pr) air electrodes for proton-conducting reversible solid oxide cells, Electrochim. Acta 267 (2018) 269. DOI: https://doi.org/10.1016/j.electacta.2018.02.053.

[17] L. Miao, J. Hou, Z. Gong, Z. Jin, W. Liu, A high-performance cobalt-free Ruddlesden-Popper phase cathode $La_{1\cdot2}Sr_{0\cdot8}Ni_{0\cdot6}Fe_{0\cdot4}O_{4+\delta}$ for low temperature proton-conducting solid oxide fuel cells, Int. J. Hydrogen Energy 44 (2019) 7531. DOI: https://doi.org/10.1016/j.ijhydene.2019.01.255.

[18] W. Li, B. Guan, L. Ma, H. Shanshan, N. Zhang, X. Liu, High performing triple-conductive $Pr_2NiO_{4+\delta}$ anode for proton-conducting steam solid oxide electrolysis cell, J. Mater. Chem. A 6 (2018) 18057. DOI: https://doi.org/10.1039/C8TA04018D.

[19] N. L. R. M. Rashid, A. A. Samat, A. A. Jais, M. R. Somalu, A. Muchtar, N. A. Baharuddin, W. N. R. Wan Isahak, Review on zirconate-cerate-based electrolytes for proton-conducting solid oxide fuel cell, Ceram. Int. 45 (2019) 6605. DOI: https://doi.org/10.1016/j.ceramint.2019.01.045.

[20] P.Tarutin, J. G. Lyagaeva, A. S. Farlenkov, A. I. Vylkov, D. M. Medvedev, Cu-substituted $La_2NiO_{4+\delta}$ as oxygen electrodes for protonic ceramic electrochemical cells, Ceram. Int. 45 (2019) 16105. DOI: https://doi.org/10.1016/j.ceramint.2019.05.127.

[21] N. Nasani, D. Ramasamy, S. Mikhalev, A. V. Kovalevsky, D. P.Fagg, Fabrication and electrochemical performance of a stable, anode supported thin $BaCe_{0.4}Zr_{0.4}Y_{0.2}O_{3-\delta}$electrolyte Protonic Ceramic Fuel Cell, J. Power Sources 278 (2015) 582. DOI: https://doi.org/10.1016/j.jpowsour.2014.12.124.

[22] V. A. Sadykov, E. Yu. Pikalova, Z. S. Vinokurov, A. N. Shmakov, N. F. Eremeev, E. M. Sadovskaya, J. G. Lyagaeva, D. A. Medvedev, V. D. Belyaeva, Tailoring the structural, thermal and transport properties of $Pr_2NiO_{4+\delta}$ through Ca-doping strategy, Solid State Ionics 333 (2019) 30. DOI: https://doi.org/10.1016/j.ssi.2019.01.014.

[23] E. P. Antonova, D. A. Osinkin, N. M. Bogdanovich, M. Yu. Gorshkov, D. I. Bronin, Electrochemical performance of $Ln_2NiO_{4+\delta}$ (Ln – La, Nd, Pr) And $Sr_2Fe_{1.5}Mo_{0.5}O_{6-\delta}$ oxide electrodes in contact with apatite-type $La_{10}(SiO_6)_4O_3$ electrolyte, Solid State Ionics 329 (2019) 82. DOI: https://doi.org/10.1016/j.ssi.2018.11.019.

[24] H. Tang, Z. Gong, Y. Wu, Z. Jin, W. Liu, Electrochemical performance of nanostructured LNF infiltrated onto LNO cathode for $BaZr_{0.1}Ce_{0.7}Y_{0.2}O_{3-\delta}$–based solid oxide fuel cell, Int. J. Hydrogen Energy 43 (2018) 19756. DOI: https://doi.org/10.1016/j.ijhydene.2018.09.008.

[25] E. Kravchenko, K. Zakharchuk, A. Viskup, J. Grins, G. Svensson, V. Pankov, A. Yaremchenko, Impact of oxygen deficiency on the electrochemicalp of K_2NiF_4-type $(La_{1-x}Sr_x)_2NiO_{4-\delta}$ oxygen electrodes, ChemSusChem 10 (2016) 600. DOI: https://doi.org/10.1002/cssc.201601340.

[26] V. A. Sadykov, E. Yu. Pikalova, A. A. Kolchugin, E. A. Filonov, E. M. Sadovskaya, N. F. Eremeev, A. V. Ishchenko, A. V. Fetisov, S. M. Pikalov, Oxygen transport properties of Ca-doped Pr_2NiO_4, Solid State Ionics 317 (2018) 234. DOI: https://doi.org/10.1016/j.ssi.2018.01.035.

[27] Z. Du, Z. Zhang, A. Niemczyk, A. Olszewska, N. Chen, K. Świerczek, H. Zhao, Unveiling the effects of A-site substitutions on the oxygen ion migration in $A_{2-x}A'_xNiO_{4+\delta}$ by first principles calculations, Phys. Chem. Chem. Phys. 20 (2018) 21685. DOI: https://doi.org/10.1039/C8CP04392B.

[28] E. Kalinina, E. Pikalova, A. Kolchugin, N. Pikalova, A. Farlenkov, Comparative study of electrophoretic deposition of doped $BaCeO_3$-based films on $La_2NiO_{4+\delta}$ and $La_{1.7}Ba_{0.3}NiO_{4+\delta}$ cathode substrates, Materials 12 (2019) 2545. DOI: https://doi.org/10.3390/ma12162545.

[29] G. Li, H. Jin, Y. Cui, L. Gui, B. He, L. Zhao, Application of a novel $(Pr_{0.9}La_{0.1})_2(Ni_{0.74}Cu_{0.21}Nb_{0.05})O_{4+\delta}$-infiltrated $BaZr_{0.1}Ce_{0.7}Y_{0.2}O_{3-\delta}$ cathode for high performance protonic ceramic fuel cells, J. Power Sources 341 (2017) 192. DOI: https://doi.org/10.1016/j.jpowsour.2016.11.008.

[30] H. Shirani-Faradonbeh, M. H. Paydar, Electrical behaviour of the Ruddlesden–Popper phase, $(Nd_{0.9}La_{0.1})_2$ $Ni_{0.75}Cu_{0.25}O_4$ (NLNC) and NLNC- x wt% $Sm_{0.2}Ce_{0.8}O_{1.9}$ (SDC) (x = 10, 30 and 50), as intermediate-temperature solid oxide fuel cells cathode, Ceram. Int. 44 (2018) 1971. DOI: https://doi.org/10.1016/j.ceramint.2017.10.140.

[31] R. Gilev, E. A. Kiseleva, V. A. Cherepanov, Oxygen transport phenomena in $(La,Sr)_2(Ni,Fe)O_4$ materials, J. Mater. Chem. A 6 (2018) 5304. DOI: https://doi.org/10.1039/C7TA07162K.

[32] R. Gilev, E. A. Kiselev, D. M. Zakharov, V. A. Cherepanov, Effect of calcium and copper/iron co-doping on defect-induced properties of La_2NiO_4-based materials, J. Alloys Compd.753 (2018) 491. DOI: https://doi.org/10.1016/j.jallcom.2018.04.178.

[33] D. A. Medvedev, J. G. Lyagaeva, E. V. Gorbova, A. K. Demin, P. Tsiakaras, Advanced materials for SOFC application: Strategies for the development of highly conductive and stable solid oxide proton electrolytes, Prog. Mater. Sci. 75 (2016) 38. DOI: https://doi.org/10.1016/j.pmatsci.2015.08.001.

[34] Y. Liu, W. Wang, X. Xu, J.-P. M. Veder, Z. Shao, Recent advances in anion-doped metal oxides for catalytic applications, J. Mater. Chem. A 7 (2019) 7280. DOI: https://doi.org/10.1039/C8TA09913H.

[35] E. Ushakov. O. V. Merkulov, A. A. Markov, M. V. Patrakeev, I. A. Leonidov, Ceramic and transport properties of halogen-substituted strontium ferrite, Ceram. Int. 44 (2018) 11301. DOI: https://doi.org/10.1016/j.ceramint.2018.03.177.

[36] N. A. Tarasova, Ya. V. Filinkova, I. E. Animitsa, Hydration and forms of oxygen-hydrogen groups in Oxyfluorides $Ba_{2-0.5x}In_2O_{5-x}F_x$, Russ. J. Phys. Chem. A 86 (2012) 1208. DOI: https://doi.org/10.1134/S0036024412080134.

[37] N. A. Tarasova, Ya. V. Filinkova, I. E. Animitsa, Electric properties of oxyfluorides $Ba_2In_2O_{5-0.5x}$ F_x with brownmillerite structure, Russ. J. Electrochem. 49 (2013) 45. DOI: https://doi.org/10.1134/S102319351301014X.

[38] N. Tarasova, I. Animitsa, T. Denisova, R. Nevmyvako, The influence of fluorine doping on short-range structure in brownmillerite $Ba_{1.95}In_2O_{4.9}F_{0.1}$, Solid State Ionics 275 (2015) 47. DOI: https://doi.org/10.1016/j.ssi.2015.02.009.

[39] N. Tarasova, I. Animitsa, Synthesis, Short-Range Structure and Hydration Processes of Oxyhalides Ba_2InO_3X (X = F, Cl, Br) with Ruddlesden-Popper Structure, Mater. Sci. Forum 916 (2018) 130. DOI: https://doi.org/10.4028/www.scientific.net/MSF.916.130.

[40] N. A. Tarasova, I. E. Animitsa, The Influence of the Nature of Halogen on the Local Structure and Intercalation of Water in Oxyhalides Ba_2InO_3X (X = F, Cl, Br), Opt. Spectrosc. 124 (2018) 163. DOI: https://doi.org/10.1134/S0030400X18020170.

[41] Y. Wang, H. Wang, T. Liu, F. Chen, C. Xia, Improving the chemical stability of $BaCe_{0.8}Sm_{0.2}O_{3-\delta}$ electrolyte by Cl doping for proton-conducting solid oxide fuel cell, Electrochem. Commun. 28 (2013) 87. DOI: https://doi.org/10.1016/j.elecom.2012.12.012.

[42] F. Su, C. Xia, R. Peng, Novel fluoride-doped barium cerate applied as stable electrolyte in proton conducting solid oxide fuel cells, J. Eur. Ceram. Soc. 35 (2015) 3553. DOI: https://doi.org/10.1016/j.jeurceramsoc.2015.05.016.

[43] H. Zhou, L. Dai, L. Jia, J. Zhu, Y. Li, L. Wang, Effect of fluorine, chlorine and bromine doping on the properties of gadolinium doped barium cerate electrolytes, Int. J. Hydrogen Energy 40 (2015) 8980. DOI: https://doi.org/10.1016/j.ijhydene.2015.05.040.

[44] Triviño-Peláez, D. Pérez-Coll, G. C. Mather, Electrical properties of proton-conducting $BaCe_{0.8}Y_{0.2}O_{3-\delta}$ and the effects of bromine addition, Acta Materialia 167 (2019) 12. DOI: https://doi.org/10.1016/j.actamat.2019.01.028.

[45] Y. Xie, N. Shi, D. Huan, W. Tan, J. Zhu, X. Zheng, H. Pan, R. Peng, C. Xia, A stable and efficient cathode for fluorine-containing proton-conducting solid oxide fuel cells, ChemSusChem 11 (2018) 3423. DOI: https://doi.org/10.1002/cssc.201801193.

[46] J. Liu, Z. Jin, L. Miao, J. Ding, H. Tang, Z. Gong, R. Peng, W. Liu, A novel anions and cations co-doped strategy for developing high-performance cobalt-free cathode for intermediate-temperature proton-conducting solid oxide fuel cells, Int. J. Hydrogen Energy 44 (2019) 11079. DOI: https://doi.org/10.1016/j.ijhydene.2019.03.001.

[47] C. Greaves, M.G. Francesconi, Fluorine insertion in inorganic materials, Cure. Opin. Solid State Mater. Sci. 3 (1998) 132. DOI: https://doi.org/10.1016/S1359-0286(98)80077-6.

[48] P. Slater, Poly(vinylidene fluoride) as a reagent for the synthesis of K_2NiF_4-related inorganic oxide fluorides, J. Fluorine Chem. 117 (2002) 43. DOI: https://doi.org/10.1016/S0022-1139(02)00166-5.

[49] G. Ehora, C. Renard, S. Daviero-Minaud, O. Mentré, New $BaCoO_{3-\delta}$ polytypes by rational substitution of O^{2-} for F^-, Chem. Mater. 19 (2007) 2924. DOI: https://doi.org/10.1021/cm070576o.

[50] O. Mentré, H. Kabbour, G. Ehora, G. Tricot, S. Daviero-Minaud, M.H. Whangbo, Anion-vacancy-induced magneto-crystalline anisotropy in fluorine-doped hexagonal cobaltites, J. Am. Chem. Soc. 132 (2010) 4865. DOI: https://doi.org/10.1021/ja100170m.

[51] M. Sturza, S. Daviero-Minaud, H. Kabbour, O. Gardoll, O. Mentré, Fluorination of iron hexagonal perovskites promoting low temperature oxygen mobility, Chem. Mater. 22 (2010) 6726. DOI: https://doi.org/10.1021/cm102724k.

[52] J. Zhu, G. Liu, Z. Liu, Z. Chu, W. Jin, N. Xu, Unprecedented perovskite oxyfluoride membranes with high-efficiency oxygen ion transport paths for low-temperature oxygen permeation, Adv. Mater. 28 (2016) 3511. DOI: https://doi.org/10.1002/adma.201505959.

[53] Y. Guo, X. Zhang, R. Wäppling, Crystal structure of $La_{1-x}Sr_xMnO_{3-2x+\delta}F_{2x}$, J. Alloy Compd. 306 (2000) 133. DOI: https://doi.org/10.1016/S0925-8388(00)00763-5.

[54] A.L. Hector, J.A. Hutchings, R.L. Needs, M.F. Thomas, M.T. Weller, Structural and Mössbauer study of Sr_2FeO_3X (X = F, Cl, Br) and the magnetic structure of Sr_2FeO_3F, J. Mater. Chem. 11 (2001) 527. DOI: https://doi.org/10.1039/b008321f.

[55] R.L. Needs, M.T. Weller, A new 2+/3+ perovskite: The synthesis and structure of $BaScO_2F$, J. Solid State Chem. 139 (1998) 422. DOI: https://doi.org/10.1006/jssc.1998.7835.

[56] N. Tarasova, I. Animitsa, Protonic transport in oxyfluorides Ba_2InO_3F and $Ba_3In_2O_5F_2$ with Ruddlesden–Popper structure, Solid State Ionics 275 (2015) 53. DOI: http://dx.doi.org/10.1016/j.ssi.2015.03.025.

[57] R.L. Needs, M.T. Weller, Structure of $Ba_3In_2O_5F_2$ by combined powder x-ray and neutron diffraction analysis: Oxide/fluoride ordering in a Ruddlesden-Popper phase, J. Chem. Soc. Dalton Trans. (1995) 3015. DOI: https://doi.org/10.1039/DT9950003015.

[58] R.L. Needs, M.T. Weller, U. Scheler, R.K. Harris, Synthesis and structure of Ba_2InO_3X (X = F, C1, Br) and Ba_2ScO_3F; oxide/halide ordering in K_2NiF_4-type structures, J. Mater. Chem. 6 (1996) 1219. DOI: https://doi.org/10.1039/JM9960601219.

[59] T. Vogt, P.M. Woodward, B.A. Hunter, A.K. Prodjosantoso, B.J. Kennedy, Sr_3MO_4F (M = Al, Ga) – A new family of ordered oxyfluorides, J. Solid State Chem. 144 (1999) 228. DOI: https://doi.org/10.1006/jssc.1999.8172.

[60] Z. Xia, R.S. Liu, Tunable Blue-green color emission and energy transfer of $Ca_2Al_3O_6F:Ce^{3+},Tb^{3+}$ phosphors for near-UV white LEDs, J. Phys. Chem. C 116 (2012) 15604. DOI: https://doi.org/dx.doi.org/10.1021/jp304722z.

[61] FullProf suite for Rietveld method Homepage. URL: https://www.ill.eu/sites/fullprof/php/downloads.html (accessed on 18 October 2019).

[62] Zirconia-318, Site of project Zirconia. URL: https://zirconiaproject.wordpress.com/devices/zirconia-318 (accessed on 18 October 2019).

[63] J. Lyagaeva, G. Vdovin, L. Hakimova, D. Medvedev, A. Demin, P. Tsiakaras, $BaCe_{0.5}Zr_{0.3}Y_{0.2-x}Yb_xO_{3-\delta}$ proton-conducting electrolytes for intermediate-temperature solid oxide fuel cells, Electrochim. Acta 251 (2017) 554. DOI: https://doi.org/10.1016/j.electacta.2017.08.149.

[64] D. Medvedev, J. Lyagaeva, G. Vdovin, S. Beresnev, A. Demin, P. Tsiakaras, A tape calendering method as an effective way for the preparation of proton ceramic fuel cells with enhanced performance, Electrochim. Acta 210 (2016) 681. DOI: https://doi.org/10.1016/j.electacta.2016.05.197.

[65] J. Lyagaeva, D. Medvedev, E. Pikalova, S. Plaksin, A. Brouzgou, A. Demin, P. Tsiakaras, A detailed analysis of thermal and chemical compatibility of cathode materials suitable for $BaCe_{0.8}Y_{0.2}O_{3-\delta}$ and $BaZr_{0.8}Y_{0.2}O_{3-\delta}$proton electrolytes for solid oxide fuel cell application, Int. J. Hydrogen Energy 42 (2017) 1715. DOI: https://doi.org/10.1016/j.ijhydene.2016.07.248.

[66] A. Tarutin, A. Kasyanova, J. Lyagaeva, G. Vdovin, D. Medvedev, Towards high-performance tubular-type protonic ceramic electrolysis cells with all-Ni-based functional electrodes, J. Energy Chem. 40 (2020) 65. DOI: https://doi.org/10.1016/j.jechem.2019.02.014.

[67] R. D. Shannon, Revised effective ionic radii and systematic studies of interatomic distances in halides and chalcogenides, Acta Crystal. A32 (1976) 751. DOI: https://doi.org/10.1107/S0567739476001551.

[68] K. Wissel, J. Heldt, P. B. Groszewicz, S.Dasgupta, H. Breitzke, M. Donzelli, A. I. Waidha, A. D. Fortes, J. Rohrer, P. R. Slater, G. Buntkowsky, O. Clemens, Topochemical fluorination of La_2NiO_{4+d}: unprecedented ordering of oxide and fluoride ions in $La_2NiO_3F_2$, Inorg. Chem. 57 (2018) 6549. DOI: https://doi.org/10.1021/acs.inorgchem.8b00661.

[69] S. M. Pikalov, L. B. Vedmid, E. A. Filonova, E. Yu. Pikalova, J. G. Lyagaeva, N. A. Danilov, A. A. Murashkina, High-temperature behaviour of calcium substituted layered neodymium nickelates, J. Alloys Compd. 801 (2019) 558. DOI: https://doi.org/10.1016/j.jallcom.2019.05.349.

[70] E. Yu. Pikalova, V. A. Sadykov, E. A. Filonova, N. F. Eremeev, E. M. Sadovskaya, S. M. Pikalov, N. M. Bogdanovich, J. G. Lyagaeva, A. A. Kolchugin, L. B. Vedmid', A. V. Ishchenko, V. B. Goncharov, Solid State Ionics 335 (2019) 53. DOI: https://doi.org/10.1016/j.ssi.2019.02.012.

[71] A. Montenegro-Hernández, J. Vega-Castillo, A. Caneiro, L. Mogni, High temperature orthorhombic/tetragonal transition and oxygen content of $Pr_{2-x}Nd_xNiO_{4+\delta}$ (x= 0, 0.3, 1, 1.7 and 2) solid solutions, J. Solid State Chem. 276 (2019) 210. DOI: https://doi.org/10.1016/j.jssc.2019.05.007.

[72] Løken, S. Ricote, S. Wachowski, Thermal and chemical expansion in proton ceramic electrolytes and compatible electrodes, Crystals 8 (2018) 365. DOI: https://doi.org/10.3390/cryst8090365.

[73] Y. Toyosumi, H. Ishikawa, K. Ishikawa, Structural phase transition of $Nd_2NiO_{4+\delta}$ ($0.106 \leq \delta \leq 0.224$), J. Alloys Compd. 408–412 (2006) 1200. DOI: https://doi.org/10.1016/j.jallcom.2004.12.201.

[74] E. Niwa, T. Nakamura, J. Misusaki, T. Hashimoto, Analysis of structural phase transition of $Nd_2NiO_{4+\delta}$ by scanning thermal measurement under controlled oxygen partial pressure, Thermochim. Acta 523 (2011) 46. DOI: https://doi.org/10.1016/j.tca.2011.04.031.

[75] M. Sakai, C. Wang, T. Okiba, H. Soga, E. Niwa, T. Hashimoto, Thermal analysis of structural phase transition behaviour of $Ln_2Ni_{1-x}Cu_xO_{4+\delta}$ (Ln = Nd, Pr) under various oxygen partial pressures, J. Therm. Anal. Calorim. 135 (2019) 2765. DOI: https://doi.org/10.1007/s10973-018-7621-0.

[76] V. V. Sereda, D. S. Tsvetkov, I. L. Ivanova, A. Yu. Zueva, Oxygen nonstoichiometry, defect structure and related properties of $LaNi_{0.6}Fe_{0.4}O_{3-\delta}$, J. Mater. Chem. A 3 (2015) 6028. DOI: https://doi.org/10.1039/c4ta05882h.

[77] R. Pelosato, G. Cordaro, D. Stucchi, C. Cristiani, G. Dotelli, Cobalt based layered perovskites as cathode material for intermediate temperature Solid Oxide Fuel Cells: A brief review, J. Power Sources 298 (2015) 46. DOI: https://doi.org/10.1016/j.jpowsour.2015.08.034.

[78] S. S. Hashim, F. Liang, W. Zhou, J. Sunarso, Cobalt-free perovskite cathodes for solid oxide fuel cells, ChemSusChem 6 (2019) 3549. DOI: https://doi.org/10.1002/celc.201900391.

[79] V.V. Kharton, A.A. Yaremchenko, A.L. Shaula, M.V. Patrakeev, E.N. Naumovich, D.I. Logvinovich, J.R. Frade, F.M.B. Marques, Transport properties and stability of Ni-containing mixed conductors with perovskite- and K_2NiF_4-type structure, J. Solid State Chem. 177 (2004) 26–37. https://doi.org/10.1016/S0022-4596(03)00261-5.

[80] S.Y. Jeon, M.B. Choi, H.N. Im, J.H. Hwang, S.J. Song, Oxygen ionic conductivity of $La_2NiO_{4+\delta}$ via interstitial oxygen defect, J. Phys. Chem. Solids 73 (2012) 656–660. https://doi.org/10.1016/j.jpcs.2012.01.006.

[81] T. Ishihara, Oxide ion conductivity in defect perovskite, Pr_2NiO_4 and its application for solid oxide fuel cells, J. Ceram. Soc. Jpn., 122 (2014) 179. DOI: https://doi.org/10.2109/jcersj2.122.179.

[82] S.-Y. Jeon, M.-B. Choi, H.-N. Im, J.-H. Hwang, S.-J.Song, Oxygen ionic conductivity of $La_2NiO_{4+\delta}$ via interstitial oxygen defect, J. Phys. Chem. Solids 73 (2012) 656. DOI: https://doi.org/10.1016/j.jpcs.2012.01.006.

[83] E. Yu. Pikalova, A. A. Murashkina, V. I. Maragou, A. K. Demin, V. N. Strekalovsky, P. E. Tsiakaras, CeO_2 based materials doped with lanthanides for applications in intermediate temperature electrochemical devices, Int. J. Hydrogen Energy 36 (2011) 6175. DOI: https://doi.org/10.1016/j.ijhydene.2011.01.132.

[84] J. Koettgen, S. Grieshammer, P. Hein, B. O. H. Grope, M. Nakayama, M. Martin, Understanding the ionic conductivity maximum in doped ceria: trapping and blocking, Phys. Chem. Chemi. Phys. 20 (2018) 14291. DOI: https://doi.org/10.1039/c7cp08535d.

[85] S. Lübke, H.D. Wiemhöfer, Electronic conductivity of gadolinia doped ceria, Ber. Bunsenges. Phys. Chem. 102 (1998) 642–649. DOI: https://doi.org/10.1002/bbpc.19981020407.

[86] D.P. Fagg, V.V. Kharton, J.R. Frade, P-Type electronic transport in $Ce_{0.8}Gd_{0.2}O_{2-\delta}$: the effect of transition metal oxide sintering aids, J. Electroceram. 9 (2002) 199–207. DOI: https://doi.org/10.1023/A:1023269326651.

[87] Y. Xiong, K. Yamaji, T. Horita, N. Sakai, H. Yokokawa, Hole and electron conductivities of 20 mol %-$REO_{1.5}$ doped CeO_2 (RE = Yb, Y, Gd, Sm, Nd, La), J. Electrochem. Soc. 151 (2004) A407–A412. DOI: https://doi.org/10.1149/1.1646149.

[88] D. Lee, H. N. Lee, Controlling oxygen mobility in Ruddlesden–Popper oxides, Materials 10 (2017) 368. DOI: https://doi.org/10.3390/ma10040368.

[89] Y. Shen, H. Zhao, X. Liu, N. Xu, Preparation and electrical properties of Ca-doped La2NiO4+δ cathode materials for IT-SOFC, Phys. Chem. Chem. Phys. 12 (2010) 15124. DOI: https://doi.org/10.1039/C0CP00261E.

[90] I. Animitsa, N. Tarasova, Ya. Filinkova, Electrical properties of the fluorine-doped $Ba_2In_2O_5$, Solid State Ionics 207 (2012) 29. DOI: https://doi.org/10.1016/j.ssi.2011.11.015.

[91] N. Tarasova, I. Animitsa, Anionic doping (F^-, Cl^-) as the method for improving transport properties of proton-conducting perovskites based on $Ba_2CaNbO_{5.5}$, Solid State Ionics 317 (2018) 21. DOI: https://doi.org/10.1016/j.ssi.2018.01.001.

[92] N. Tarasova, I. Animitsa, The influence of anionic heterovalent doping on transport properties and chemical stability of F-, Cl-doped brownmillerite $Ba_2In_2O_5$, J. Alloys Compd. 739 (2018) 353. DOI: https://doi.org/10.1016/j.jallcom.2017.12.317.

[93] N. Tarasova, I. Animitsa, The influence of fluorine doping on transport properties in the novel proton conductors $Ba_4In_2Zr_2O_{11-0.5x}F_x$ with perovskite structure, Solid State Sciences 87 (2019) 87. DOI: https://doi.org/10.1016/j.solidstatesciences.2018.11.013.

[94] N. Tarasova, I. Animitsa, Fluorine-doped oxygen-ion conductors based on perovskite $Ba_4In_2Zr_2O_{11}$, J. Fluor. Chem. 216 (2018) 107 DOI: https://doi.org/10.1016/j.jfluchem.2018.10.013.

[95] S. Presto, C. Artini, M. Pani, M. M. Carnasciali, S. Massardo, M. Viviani, Ionic conductivity and local structural features in $Ce_{1-x}Sm_xO_{2-x/2}$, Phys. Chem. Chem. Phys. 20 (2018) 28338. DOI: https://doi.org/10.1039/C8CP04186E.

[96] M. Saccoccio, T.H. Wan, C. Chen, F. Ciucci, Optimal regularisation in distribution of relaxation times applied to electrochemical impedance spectroscopy: ridge and lasso regression methods – a theoretical and experimental study, Electrochim. Acta 147 (2014) 470–482. DOI: https://doi.org/10.1016/j.electacta.2014.09.058.

[97] F. Ciucci, C. Chen, Analysis of Electrochemical Impedance Spectroscopy Data Using the Distribution of Relaxation Times: A Bayesian and Hierarchical Bayesian Approach, Electrochim. Acta 167 (2015) 439–454. DOI: https://doi.org/10.1016/j.electacta.2015.03.123.

[98] Grimaud, F. Mauvy, J. M. Bassat, S. Fourcade, L. Rocheron, M. Marrony, J. C. Grenier, Hydration properties and rate determining steps of the oxygen reduction reaction of perovskite-related oxides as H^+-SOFC cathodes, J. Electrochem. Soc. 159 (2012) B683. DOI: https://doi.org/10.1149/2.101205jes.

[99] Grimaud, F. Mauvy, J. M. Bassat, S. Fourcade, M. Marrony, J. C. Grenier, Hydration and transport properties of the $Pr_{2-x}Sr_xNiO_{4+\delta}$compounds as H^+-SOFC cathodes, J. Mater. Chem. 22 (2012) 16017. DOI: https://doi.org/10.1039/c2jm31812a.

[100] J. Dailly, F. Mauvy, M. Marrony, M. Pouchard, J.-C. Grenier, Electrochemical properties of perovskite and A_2MO_4-type oxides used as cathodes in protonic ceramic half cells, J. Solid State Electrochem. 15 (2011) 245. DOI: https://doi.org/10.1007/s10008-010-1188-4.

[101] J. Dailly, S. Fourcade, A. Largeteau, F. Mauvy, J. C. Grenier, M. Marrony, Perovskite and A_2MO_4-type oxides as new cathode materials for protonic solid oxide fuel cells, Electrochim. Acta 55 (2010) 5847. DOI: https://doi.org/10.1016/j.electacta.2010.05.034.

[102] E. G. Kalinina, E. Yu. Pikalova, A. A. Kolchugin, Formation of Bilayer Thin-Film Electrolyte on Cathode Substrate by Electrophoretic Deposition, Russ. J. Electrochem. 54 (2018) 723. DOI: https://doi.org/10.1134/S1023193518090045.

[103] M. Heinzmann, A. Weber, E. Ivers-Tiffée, Advanced impedance study of polymer electrolyte membrane single cells by means of distribution of relaxation times, J. Power Sources 402 (2018) 24. DOI: https://doi.org/10.1016/j.jpowsour.2018.09.004.

[104] P. Batocchi, F. Mauvy, S. Fourcade, M.Parco, Electrical and electrochemical properties of architectured electrodes based on perovskite and A_2MO_4-type oxides for Protonic Ceramic Fuel Cell, Electrochim. Acta 145 (2014) 1. DOI: https://doi.org/10.1016/j.electacta.2014.07.001.

[105] E. Yu. Pikalova, A. A. Kolchugin, V. A. Sadykov, E. M. Sadovskaya, E. A. Filonov, N. F. Eremeev, N. M. Bogdanovich, Structure, transport properties and electrochemical behaviour of the layered lanthanide nickelates doped with calcium, Int. J. Hydrogen Energy 43 (2018) 17373. DOI: https://doi.org/10.1016/j.ijhydene.2018.07.115.

[106] V. Vibhu, A. Rougier, C. Nicollet, A. Flura, J.-C. Grenier, J.-MarcBassat, $La_{2-x}Pr_xNiO_{4+\delta}$ as suitable cathodes for metal supported SOFCs, Solid State Ionics 278 (2015) 32. DOI: https://doi.org/10.1016/j.ssi.2015.05.005.

[107] S. N. Marshenya, B. V. Politov, D. A. Osinkin, A. Yu. Suntsov, I. A. Leonidov, V. L. Kozhevnikov, Advanced electrochemical properties of $Pr_{0.9}Y_{0.1}BaCo_{1.8}Ni_{0.2}O_{6-\delta} - Ce_{0.8}Sm_{0.2}O_{1.9}$ composite as cathode material for IT–SOFCs, J. Alloys Compd. 779 (2019) 712. DOI: https://doi.org/10.1016/j.jallcom.2018.11.255.

[108] Tarutin, J. Lyagaeva, A. Farlenkov, S. Plaksin, G. Vdovin, , A. Demin, D. Medvedev, A Reversible Protonic Ceramic Cell with Symmetrically Designed $Pr_2NiO_{4+\delta}$-Based Electrodes: Fabrication and Electrochemical Features, Materials 12 (2018) 118. DOI: https://doi.org/10.3390/ma12010118.

[109] N. Kochetova, I. Animitsa, D. Medvedev, A. Demin, P. Tsiakaras, Recent activity in the development of proton-conducting oxides for high-temperature applications, RSC Adv. 6 (2016) 73222. DOI: https://doi.org/10.1039/C6RA13347A.

[110] D. Huan, N. Shi, Lu Zhang, W. Tan, Y. Xie, W. Wang, C. Xia, R. Peng, Y. Lu, New, efficient, and reliable air electrode material for proton-conducting reversible solid oxide cells, ACS Appl. Mater. Interfaces 10 (2018) 1761. DOI: https://doi.org/10.1021/acsami.7b16703.

[111] S. Yang, Y. Lu, Q. Wang, C. Sun, X. Ye, Z. Wen, Effects of porous support microstructure enabled by the carbon microsphere pore former on the performance of proton-conducting reversible solid oxide cells, Int. J. Hydrogen Energy 43 (2018) 20050. DOI: https://doi.org/10.1016/j.ijhydene.2018.09.011.

[112] S. Yang, S. Zhang, C. Sun, X. Ye, Z. Wen, Lattice incorporation of Cu^{2+} into the $BaCe_{0.7}Zr_{0.1}Y_{0.1}Yb_{0.1}O_{3-\delta}$ electrolyte on boosting its sintering and proton-conducting abilities for reversible solid oxide cells, ACS Appl. Mater. Interfaces 10 (2018) 42387. DOI: https://doi.org/10.1021/acsami.8b15402.

[113] D. Huan, W. Wang, Y. Xie, N. Shi, Y. Wan, C. Xia, R. Peng, Y. Lu, Investigation of real polarisation resistance for electrode performance in proton-conducting electrolysis cells, J. Mater. Chem. A 6 (2018) 18508. DOI: https://doi.org/10.1039/C8TA06862C.

[114] S. Choi, T. C. Davenport, S. M. Haile, Protonic ceramic electrochemical cells for hydrogen production and electricity generation: exceptional reversibility, stability, and demonstrated faradaic efficiency, Energy Environ. Sci. 12 (2019) 206. DOI: https://doi.org/10.1039/c8ee02865f.

[115] W. Li, B. Guan, L. Ma, H. Tian, X. Liu, Synergistic coupling of proton conductors $BaZr_{0.1}Ce_{0.7}Y_{0.1}Yb_{0.1}O_{3-\delta}$ and $La_2Ce_2O_7$ to create chemical stable, interface active electrolyte for steam electrolysis cells, ACS Appl. Mater. Interfaces 11 (2019) 18323, DOI: https://doi.org/10.1021/acsami.9b00303.

[116] N. Danilov, J. Lyagaeva, G. Vdovin, D. Medvedev, Multifactor performance analysis of reversible solid oxide cells based on proton-conducting electrolytes, Appl. Energy 237 (2019) 924. DOI: https://doi.org/10.1016/j.apenergy.2019.01.054.

[117] J. Kim, A. Jun, O. Gwon, S. Yoo, M. Liu, J. Shin, T.-H. Lim, G. Kim, Hybrid-solid oxide electrolysis cell: A new strategy for efficient hydrogen production, Nano Energy 44 (2018) 121. DOI: https://doi.org/10.1016/j.nanoen.2017.11.074.

[118] C. Zhou, J. Sunarso, Y. Song, J. Dai, J. Zhang, B. Gu, W. Zhou, Z. Shao, New reduced-temperature ceramic fuel cells with dual-ion conducting electrolyte and triple-conducting double perovskite cathode, J. Mater. Chem. A 7 (2019) 13265. DOI: https://doi.org/10.1039/c9ta03501j.

[119] Institute of High Temperature Electrochemistry of the Ural Branch of the Russian Academy of Sciences, http://www.ihte.uran.ru/?page_id=3142 (accessed on 18 October 2019).

Fluorine-containing oxygen electrodes of the nickelate family for proton-conducting electrochemical cells

Artem P. Tarutin[a,b], Gennady K. Vdovin[a],
Dmitry A. Medvedev[a,b,*], Aleksey A. Yaremchenko[c,*]

[a] Laboratory of Electrochemical Devices Based on Solid Oxide Proton Electrolytes, Institute of High Temperature Electrochemistry, Yekaterinburg 620137, Russia
[b] Ural Federal University, Yekaterinburg 620002, Russia
[c] CICECO – Aveiro Institute of Materials, Department of Materials and Ceramic Engineering, University of Aveiro, 3810-193 Aveiro, Portugal
[*]Corresponding authors, e-mails: dmitrymedv@mail.ru (D.A. Medvedev) and ayaremchenko@ua.pt (A.A. Yaremchenko).

Author Contribution Statement

Conceptualization: D.M.; Methodology: A.T., G.V., D.M. and A.Y.; Validation: D.M.; Formal analysis: A.T., D.M. and A.Y.; Investigation: A.T., G.V. and D.M.; Resources: A.T. and G.K.; Writing – original draft preparation: A.T., D.M. and A.Y.; Writing – review & editing: D.M.; Visualization: A.T.; Supervision: D.M.; Project administration: D.M.; Funding acquisition: A.T., D.M. and A.Y.

Declaration of interests

☒ The authors declare that they have no known competing financial interests or personal relationships that could have appeared to influence the work reported in this paper.

☐The authors declare the following financial interests/personal relationships which may be considered as potential competing interests: